Optimization of Nanoscale Waveguide Taper and Bend Geometries

THOMAS HOEKMAN

McGill University, Montreal CA

March 2018

A thesis submitted to McGill University in partial fulfillment of the requirements of the degree of Masters of Materials Engineering

Table of Contents

Abstract

Sustained growth of commercially viable applications for integrated photonic technologies requires the performance of core optical components be improved without sacrificing manufacturability or introducing unreasonable design lead times. In this thesis, the geometries of two fundamental components of photonic integrated circuits were optimized under a wide variety of design conditions, and the results of these optimizations were studied to improve our understanding of the interplay between waveguide geometry and electromagnetic mode conversion at small scales. First, the concept of a constant loss inverted taper was presented and its geometry for common nanoscale waveguide structures was studied using coupled mode theory. The underlying concepts behind this device were also revisited and further investigated through functional analysis. A new normalization and fitting procedure was presented, which led to a global equation for the constant loss taper profile. Second, curved waveguide bends in orthogonal waveguide couplers were simulated via finite difference time domain and optimized. The effect of the device footprint on the optimal shape and performance was investigated and intuitive trends were found for the bend parameters. These trends were closely related to historical concepts of transition and bending losses in curved structures and, more specifically, the difference in the scaling behavior for these two attenuation mechanisms.

Résumé de thèse

Une croissance soutenue des applications commerciales viables pour les technologies photoniques intégrées requière un perfectionnement de performances des principaux composants optiques sans que soit sacrifiée leur manufacturabilité et sans introduire des délais de conception déraisonnables. Dans cette thèse nous présentons des optimisations pour deux composants fondamentaux des circuits intégrés photoniques. Nous en étudions les résultats dans le but d'améliorer notre compréhension des interactions entre la géométrie des guides d'ondes et la conversion de mode électromagnétique à petites échelles Dans un premier temps nous présentons le concept d'entonnoir inversé à pertes constantes et nous étudions avec la théorie des modes couplés sa géométrie pour les structures de guides d'onde nanométriques communes. Nous revoyons et nous approfondissons aussi la théorie fondamentale derrière ce dispositif au travers d'une analyse fonctionnelle. Nous présentons une nouvelle procédure de normalisation et d'adaptation qui conduit à une équation globale pour la géométrie des entonnoirs inversé à pertes constantes.

Dans un second temps nous simulons et nous optimisons les coupleurs de guides d'ondes orthogonaux en utilisant la méthode de calcul de différences finies dans le domaine temporel. Nous investiguons l'influence de l'empreinte du dispositif sur la forme optimale et sa performance. Nous mettons aussi à jour des tendances intuitives pour les paramètres optimisés des courbes. Ces tendances sont étroitement liées aux concepts historiques de pertes dues à soit des transitions ou des courbes. De façon plus spécifique, la géométrie optimale est le résultat de différences dans les comportements d'échelle pour ces deux mécanismes d'atténuation.

Acknowledgments

I would like to thank my friends and family for their support during the process of writing this thesis. Also, I'd like to specifically thank Laura Ong for helping to edit this thesis and Patricia Hoekman for help summarizing the thesis in French. Also, this research was enabled in part by support provided by the McGill HPC Guillimin (www.hpc.mcgill.ca) and Compute Canada (www.computecanada.ca). Finally, I am very grateful to my supervisor Prof. Nate Quitoriano for his valuable mentorship and guidance over the course of my undergraduate and graduate degrees.

Preface

The concept of optical data transmission can be traced back to the inventors Claude Chappe and Alexander Graham Bell in the 18th and 19th centuries respectively, as they both patented communication systems that operated using light rather than electricity [1]. However, active scientific investigation into the subject only began in the 20th century, when researchers such as Van Heel [2] and Hopkins [3] began characterizing the performance of the first optical fibers. The first planar optical waveguides were fabricated in the 1960s, and three-dimensional waveguides were developed a decade later. The primary goal for these early studies was to increase signal bandwidth in transmission lines [4, 5]. Half a century of research building on these findings resulted in optimized optical material properties, fiber geometries, and signal processing methods, effectively realizing Chappe and Bell's vision of optical communication networks. Optics have displaced electronics in our modern information infrastructure at the scales of continents, datacenters, and even the home.

Considering these developments, the logical continuation for research is to pursue optical communication technologies at smaller length scales where electronics still dominate, most notably in integrated circuits. In fact, it has been well established that optical interconnects, with their potential for high bit rates, minimal losses, low weight, and immunity to electromagnetic interference, would be a promising solution to many problems facing modern computing, which currently relies on copper interconnects [4-6]. Furthermore, improvements in photonic devices for signal gain, modulation, and other signal processing operations already threaten the market for certain electronic devices. The significant potential for optics on-chip has been recognized by several established members of industry. Intel founded its Photonics Technology Lab in 2002 to pursue commercialization of integrated photonics and Hewlett Packard is actively developing "The Machine", which implements optical interconnects and memristor technology in a next generation computer. The promise of photonic systems has also resulted in more recent ventures such as Infinera and Lumentum, which specialize in applications of photonic technologies to network communications.

A general goal in the development of photonic devices is the reduction of losses. Attenuation at any stage of transmission through an optical network results in signal quality degradation and can lead to increased energy usage. This is because the initial signal power must be increased to maintain a required signal to noise ratio at the signal's destination. Furthermore, radiated light from an integrated waveguide may also have the negative effect of interfering with normal operation of other devices on chip. For example, this may occur through cross talk with other optical waveguides [7].

Two examples of simple photonic devices where incurred losses can have a significant effect on overall performance are fiber-to-chip couplers and waveguide bends. Fiber-to-chip couplers are used to transfer optical signals from fiber optics to integrated waveguides. This process involves a significant reduction in the size of the propagating optical mode, from a mode field diameter of roughly 20 μm to below 1 μm [8]. Meanwhile, waveguide bends are inevitably required to compactly package integrated photonic circuits. Due to the ubiquity of both devices, even a minor decrease in their respective losses would have a significant effect on the performance of photonic chips.

In this thesis, improved fiber-to-chip couplers and bends will be designed by leveraging high performance computer clusters and parallelized electromagnetic simulations. These simulations will numerically solve for the propagating optical modes in the devices of interest from Maxwell's equations[1] [9]. This set of four equations is presented below (Eqs. 1), alongside their simplified form (Eqs. 2). The simplified form is applicable when the materials considered are non-conductive ($\sigma = 0$), non-magnetic ($\mu = \mu_0$), isotropic, and operate in a linear regime ($D = \varepsilon E$). Here the dielectric constant (ε) and other properties are a function of position. Overall, Maxwell's equations describe the behavior of the electric (E) and magnetic (H) fields of light as they relate to the electric displacement vector (D) and magnetic flux density vector (B). Below, ρ_v denotes the charge density, which is zero for a dielectric, and J represents the current density vector.

$$\begin{gathered} \nabla \cdot D = \rho_v \\ \nabla \cdot B = 0 \\ \nabla \times E = -\frac{\partial B}{\partial t} \\ \nabla \times H = -\frac{\partial D}{\partial t} + J \end{gathered} \tag{Eqs. 1}$$

$$\begin{gathered} \nabla^2 E = \mu\sigma\frac{\partial E}{\partial t} + \mu\varepsilon\frac{\partial^2 E}{\partial^2 t} \\ \nabla^2 H = \mu\sigma\frac{\partial H}{\partial t} + \mu\varepsilon\frac{\partial^2 H}{\partial^2 t} \end{gathered} \tag{Eqs. 2}$$

The solutions to Maxwell's equations form two orthogonal sets of functions, which represent the transverse electric (TE) and transverse magnetic (TM) modes present in the waveguide. These are the modes where either the electric or magnetic field components are solely in the transverse directions (E_z or $H_z = 0$). Figure 1 shows the two fundamental modes for a 500 nm × 220 nm strip waveguide with a SiO_2 cladding. Note that due to the waveguide geometry,

[1] Here a mode is defined as an independent electromagnetic field pattern present within a waveguide that forms a solution to Maxwell's equations.

the TM mode is less confined within the core than the TE mode. Many research groups have pointed out that these asymmetries in standard waveguide geometries results in different coupling behavior for TE and TM modes, the implication being that devices are often optimized either TE or TM light [8, 10-13]. In this thesis, TE modes will be primarily considered as these are generally of interest in the 220nm silicon-on-insulator (SOI) platform [14], though similar analysis and trends would be applicable to TM modes.

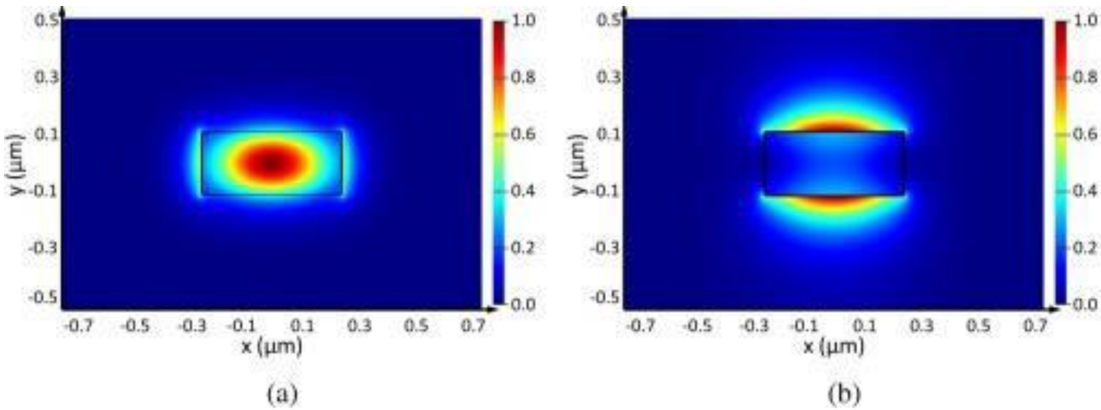

Figure 1 Fundamental (a) TE and (b) TM modes in rectangular silicon 220 nm x 500 nm waveguide surrounded by silica cladding [7].

The modes shown in Figure 1 were found by solving Maxwell's equations numerically. Frequency or time domain approaches could be used for this task. Frequency domain methods are usually best at finding the band structures and mode profiles of a given dielectric structure, but time domain models can help understand how these modes propagate and interact in the waveguide dynamically [15]. In the discussions that follow both techniques will be used: coupled mode theory will be used to study propagation through three-dimensional waveguide tapers while bends will be analyzed through finite difference time domain (FDTD) methods. Constrained geometrical optimization routines will use these methods to decrease losses incurred during propagation through both types of devices. Throughout the design process, emphasis will be placed on searching for structures that are feasible from a fabrication perspective, meaning that they are relatively easy to make and integrate into existing manufacturing pipelines.

Chapter 1: Development of a Global Fitting Equation for the Constant Loss Inverted Taper

Introduction

Coupling of optical modes present in optical fibers with those guided within integrated waveguides is a challenging practical problem as waveguide couplers designed for this task must convert spatially diffused optical modes present in fiber optics to highly confined, sub-micron optical modes present in integrated waveguides on-chip. This allows for the transfer of information from fiber optic networks to photonic devices, which are a critical building block in the optical communications technology roadmap.

The design of fiber-to-chip optical waveguide couplers is concerned with overcoming the large mode-mismatch present between fiber optics and integrated waveguides while minimizing fabrication cost, footprint, and coupling loss. Figure 2 shows example fiber optic and integrated waveguides that must be connected. If these were simply butt coupled the transmission efficiency from the fiber to the waveguide on-chip would be roughly 0.1% [16]. The use of a fiber-to-chip waveguide coupler may increase this efficiency to well above 90% [8, 12, 17, 18], thereby enabling the use of optical interconnects for communication between chips, or allowing for multiscale photonics systems by efficiently connecting integrated photonic devices with other components.

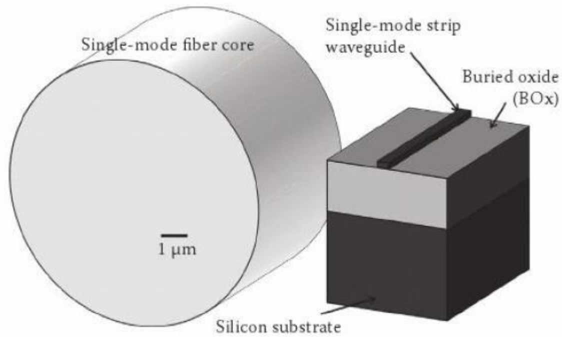

Figure 2 Single-mode optical fiber core (silica) on left and integrated silicon on insulator waveguide (Si) on right [16].

Increasingly, industry uses an inverted taper structure as a fiber-to-chip coupler because of the large bandwidth of these devices compared to grating couplers, which are often optimal for only one wavelength [16]. In an inverted taper coupler, the single-mode strip waveguide shown in Figure 2 has a smaller width at the interface with the fiber core, around 200 nm or less [8, 16, 18]. The waveguide width gradually tapers from this small tip width at the fiber interface to the width of the integrated waveguide as we move along the propagation direction. Naturally, for this process to occur efficiently the core of the single mode optical fiber must be aligned with that of an integrated waveguide, a non-trivial task that is an active area of research [19]. Relative to standard tapers and diffractive couplers, the inverted taper coupler design reduces footprint and increases bandwidth by exploiting the broadband increase in the effective mode area (EMA) when the waveguide dimension becomes much smaller than the wavelength. This phenomenon is shown in Figure 3, where a typical plot of the EMA is presented for a linear inverted taper in the case with input wavelength of 1550 nm [8]. The definition of the EMA is presented in (Eq. 3), where S_z is the component of the Poynting vector in the propagation direction and $dA = dxdy$ is the differential area element.

$$EMA = \left(\int\int S_z dA\right)^2 \Big/ \int\int S_z^2 dA \qquad \text{(Eq. 3)}$$

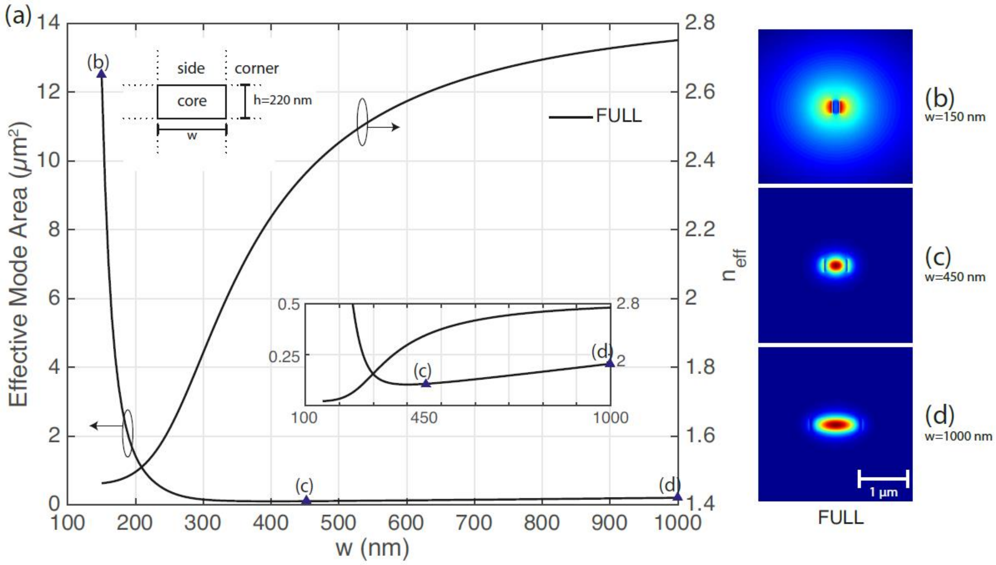

Figure 3 Effective Mode Area as a function of waveguide width for variable material systems and rectangular waveguide heights [8].

In the above figure two regimes are present, separated by a turning point at a critical waveguide width (≈ 450 nm) labeled (c) in Figure 3, most easily seen in the inset. For widths larger than this point the lateral spread of the guided mode depends roughly linearly on the waveguide dimension while the mode's vertical spread (in the vertical direction Figure 3 b – d) remains nearly constant. However, as the waveguide dimension decreases below point (c), we enter a rapid mode expansion regime where the core is no longer capable of confining the electromagnetic field. Importantly, in this regime the mode expansion occurs in both the lateral and the vertical direction. This allows for efficient conversion between the radially symmetric and diffused modes present in circular-cross-section optical fibers and the confined, 2-fold symmetric modes present in rectangular waveguides.

Tapering waveguide structures and their alternatives have been studied since the late 1960s, with researchers applying a variety of modeling approaches to optimize their performance. A survey of the literature will follow in which we shall see that previous studies have largely focused on specific use cases. Optimized taper profiles have been reported over a narrow parameter space as a result. For example, a typical taper design study will report an optimized width profile for a specific material system, device footprint, and waveguide geometry. This limits the practical application of the results as the full optimization process must be repeated by those wishing to implement the inverted taper coupler under different conditions. In addition, several complex inverted taper designs have been proposed involving several waveguide layers or multiple material systems. While interesting, these studies also have limited impact in industry due to the difficulties involved in fabrication.

There have, however, been studies presenting general design principles for taper design that are more widely implemented. Three notable examples are the Milton and Burns' adiabatic taper angle [20], Marcuse's analytical studies of power in tapering waveguides [21, 22], and Baets' work on the influence of the normalized width and effective taper angle [23, 24]. Unfortunately, these studies relied on approximations that limit their application in modern devices. The slab waveguide approximation was often used and, like all methods that reduce the dimensionality of the problem, this approach fails to accurately model rectangular cross section waveguides that are commonly used on modern photonic chips[2].

[2] The slab waveguide approximation is incapable of describing waveguiding behavior in three dimensions, and it has similarly been shown that 2.5D approximations yield distinctly different mode shapes than those found in full 3D simulations [8].

.

Therefore, we lack robust and quantitative design guidelines for the derivation of optimal inverted taper width profiles for modern fiber-to-chip couplers that nearly always couple into integrated waveguides with rectangular cross section. As a result, most experimental inverted taper studies have implemented simple linear and parabolic tapers, which are not necessarily optimal as shall be seen in the discussion that follows. This thesis chapter will attempt to address this gap in available knowledge by deriving optimal inverted taper profiles for a range of refractive indices and waveguide heights.

Literature Review

Studies on the dependence of electromagnetic mode profiles on geometry and material parameters date back to the earliest days of optics. Numerous investigations have explored the effect of changing the width, height, material, and other factors on the electromagnetic mode profiles [25-27]. Studies into tapered waveguides have also been widely published. Early studies by Marcuse, Milton, and others in the 1970s and 1980s focused on analytical treatments of tapered slab waveguides [20-22, 28]. Due to limited computational resources, simplified structures were examined, often slab waveguide tapers with widths on the order of one micron. Later, common modeling techniques such as two-dimensional coupled mode theory [29], beam propagation method [30], and finite difference [31, 32] analysis would be used to simulate tapered structures. Most researchers implemented spatial frequency domain models, which did not discretize Maxwell's equations in time steps, instead using frequency and position as the discretized variables.

At the onset of tapered waveguide research Marcuse presented the first derivation showing that a horn shaped taper, where the rate of waveguide expansion increases with propagation distance, was best for a slab waveguide system and outperformed a linear taper [28]. This paper, and later ones by Marcuse, also featured the use of a staircase approximation to a tapered waveguide structure where the loss at each step was estimated via coupled amplitude equations [21]. Building on this work, Milton et al. developed the first analytical design rule for tapered waveguides in 1977 [20]. In this paper, Milton posited that a taper would behave adiabatically if the local taper angle (Ω) was smaller than a critical value called an adiabatic tapering angle. The expression for this parameter is shown in (Eq. 4), where *w* is the waveguide width and $\lambda_g = \lambda / n_{eff}$ is the fundamental mode wavelength. This equation was derived by requiring that the tapering rate must be slower than the diffraction spreading of the lowest order mode. Love et al. would also later study the concept of an adiabatic tapering angle [33].

$$\Omega < \frac{\lambda_g}{w} \qquad \text{(Eq. 4)}$$

Shortly after Milton, Baets et al. presented two new parameters for taper design in one of the first fully numerical studies in this field [23]. Various taper width profiles were compared under the assumption that the tapers behaved adiabatically, meaning that the modes changed slowly. Using the beam propagation method (BPM), Baets found that the radiation loss in a waveguide taper was dependent on two parameters: a normalized width parameter (V_m) and the effective taper angle (θ_{eff}). Expressions for these parameters are listed below in (Eqs. 5). Here *w* again represents the taper width.

$$V_m = \sqrt{w_{in} w_{out}}$$
$$\sin(\theta_{eff}) = \frac{\sin(\theta)}{\sqrt{n_{core}^2 - n_{clad}^2}} \qquad \text{(Eqs. 5)}$$

Baets analyzed the parameter space of these two variables for linear tapers, finding that for large normalized widths small effective angles should be chosen to minimize losses. Interestingly, Baets went on to design improved taper shapes, finding a quadratic form for the taper, similarly to Marcuse [21]. The study also notes that the optimal slab waveguide taper would have constant radiation losses throughout the conversion process. This is the first time a constant loss condition is alluded to in waveguide taper literature. In research that followed this paper, it was common to design tapers such that they had a constant normalized parameter (V_m) throughout.

In the 1980s and 1990s experimental and more complex theoretical studies built on the work by Baets, Milton, Marcuse et al. However, no novel and influential guidelines for taper geometry were presented. Instead the focus shifted towards numerical optimization and improved modeling techniques and increased computational resources. Tapered waveguide simulations progressed with the work of Haes [24], Lee [34], Sewell [35], Hermansson [36, 37] and their collaborators who developed numerical techniques and improved discretization methods. These methods were used to derive optimal taper width profiles in studies by Yanagawa [38], Suchoski [29], Lu [32] and others. However most of this research remained focused on two-dimensional modeling methods, which limits its practical use today. Also, an important fact to note is that standard tapers, not inverted tapers, were of interest at the time due to fabrication limitations.

The first inverted taper studies would occur in the new millennium. Shoji et al. performed one such study in 2002 [10], presenting the idea that rapid mode expansion at low waveguide widths could be used for coupling optical fibers to waveguides on chip. This approach was then adopted by other researchers who achieved ≤ 1 dB coupling losses [8, 39]. This result represented an order of magnitude improvement over alternative in-plane couplers with the same length. Studies would also show that inverted tapers exhibit excellent coupling bandwidth at small footprint relative to competing coupling techniques [16, 18, 40].

Three-dimensional taper simulations also became widespread near the turn of the century, as increased computation capabilities allowed for modeling of rib waveguides and other complex structures. These simulations provided a better way to study and optimize the coupling behavior of light through tapers, accurately capturing the effect of rib waveguide geometry on different polarizations. Researchers such as Almeida et al. and Ren et al. used 3D FDTD and the BPM to compare linear, exponential, and parabolic taper profiles, finding that parabolic tapers had improved performance [12, 41]. Three-dimensional simulations also led to several studies suggesting that multi-layer tapers should be used to improve performance [13, 42, 43]. This was just one of many proposed structures for inverted taper couplers that were often prohibitively complicated or expensive to fabricate and integrate.

During this time, more advanced optimization techniques emerged. Zou et al. and Spuhler et al. used genetic algorithms to optimize waveguide tapers [11, 39]. Also, a return to designing waveguide tapers from first principles took place when Fu et al. performed an FDTD optimization study based on the Milton and Burns adiabatic taper angle criterion [44], and later when Horth et al. developed a novel constant loss approach to designing adiabatic tapers [8]. The structure proposed by Horth et al. emerged from a Lagrangian treatment of the mode conversion process. An inverted taper coupler as shown schematically in Figure 4 was considered, where an instantaneous loss, α, is present at each position z. If parameters such as the core index n_c, cladding index $n_{c\ell}$, and waveguide height h remain constant throughout the taper, then α will depend on the instantaneous width w and its spatial derivative $\frac{\partial w}{\partial z} = w'$. The total loss L in the taper may then be expressed as the functional in (Eq. 6), where z represents the position along the taper's length. The task of finding the path $w(z)$ which minimized the functional then reduces to solving the Euler-Lagrange equation for this system, (Eq. 7). Here we have aliased $\frac{\partial\alpha}{\partial w}$ as α_w and $\frac{\partial\alpha}{\partial w\prime}$ as $\alpha_{w\prime}$.

$$L = \int_0^Z \alpha(w, \mathrm{w}', z)dz \qquad \text{(Eq. 6)}$$

$$\begin{aligned} &\alpha_w(w, w', z) - \frac{d}{dz}\alpha_{w\prime}(w, w', z) = 0 \\ &\text{where: } \alpha_w = \frac{\partial\alpha}{\partial w}, \qquad \alpha_{w\prime} = \frac{\partial\alpha}{\partial w'} \end{aligned} \qquad \text{(Eq. 7)}$$

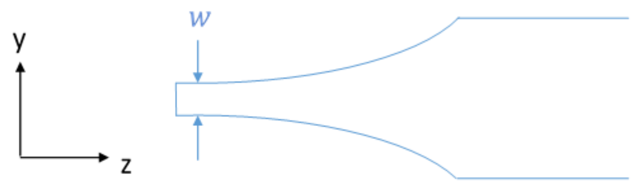

Figure 4 Schematic of inverted taper problem

Horth assumed that there was negligible attenuation when propagating through a straight waveguide, a valid assumption when considering the typical length scale of an inverted taper coupler. In this case the instantaneous loss would not explicitly depend upon position and the Beltrami identity may be used to yield the simple solution shown in (Eq. 8).

$$\alpha = w'\alpha_w = c \qquad \text{(Eq. 8)}$$

Here c is a constant, which implies that a taper with constant loss is at least a local minimum in our optimization problem. Inverted taper profiles with constant α will herein referred to as constant-loss tapers (CLTs).

Modeling

A Lagrangian Approach to Taper Design

Following the derivation of the constant loss solution to the taper coupler design problem, there remains the question of whether this solution represents a local or global minimum. This was not fully addressed in Horth et al. If the integrand α in (Eq. 6), which represents the instantaneous loss within the waveguide along the propagation direction, is convex for all continuous and monotonically increasing taper profiles, then the functional L would also have to be convex [45]. The implication of such a result would be that the constant loss solution is a global minimum to the optimization problem. Here convexity is defined as any function $f(x)$ were the condition in (Eq. 9) is met.

$$f(\lambda x_1 + (1-\lambda)x_2) \leq \lambda f(x_1) + (1-\lambda)f(x_2) \;\; \forall\, x_1, x_2 \in \mathbb{R}$$
$$\text{where: } 0 < \lambda < 1 \qquad \text{(Eq. 9)}$$

There are signs that this may be the case, at least over the interval of interest. For a 3D rectangular waveguide it is not possible to find analytical expressions for α as we cannot solve Maxwell's equations analytically for such structures. However, numerical modeling can be used to solve for the guided modes, and these can be used to perform a precursory functional analysis over the subspace of interest. Figure 5 illustrates how the step loss α_{step}, which herein refers to the loss incurred at a step perturbation in the width of a waveguide, scales with (a) the size of width perturbation at a given input width and (b) the size of the input width for a given width perturbation. The step loss is a discrete approximation of α in a tapered waveguide and was calculated from the overlap integral in (Eq.10), where $E_{i,o}$ and $H_{i,o}$ are the fundamental modes of the input and output waveguides.

$$\eta = \frac{\left|\int\int E_i \times H_o^*\right|^2}{\left|\int\int E_i \times H_i^*\right| \cdot \left|\int\int E_o \times H_o^*\right|} \qquad \text{(Eq.10)}$$

(a)

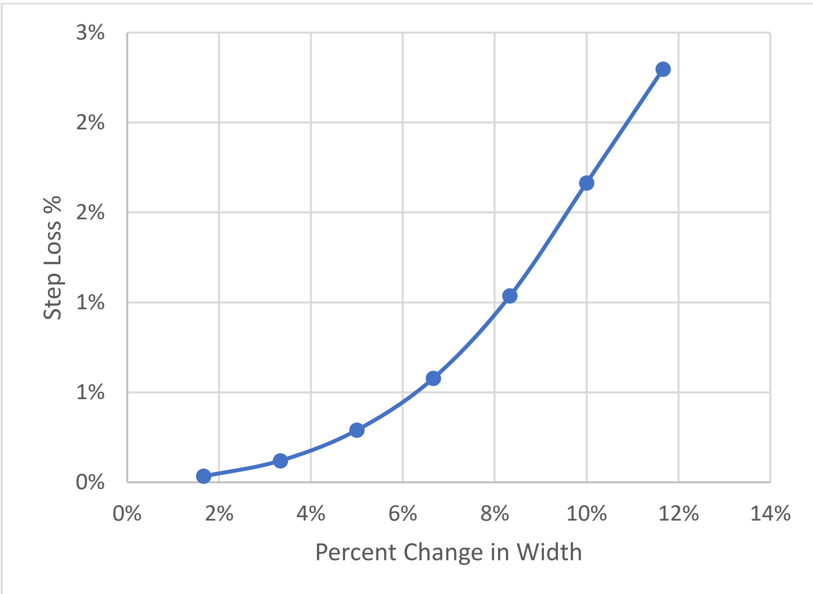

(b)

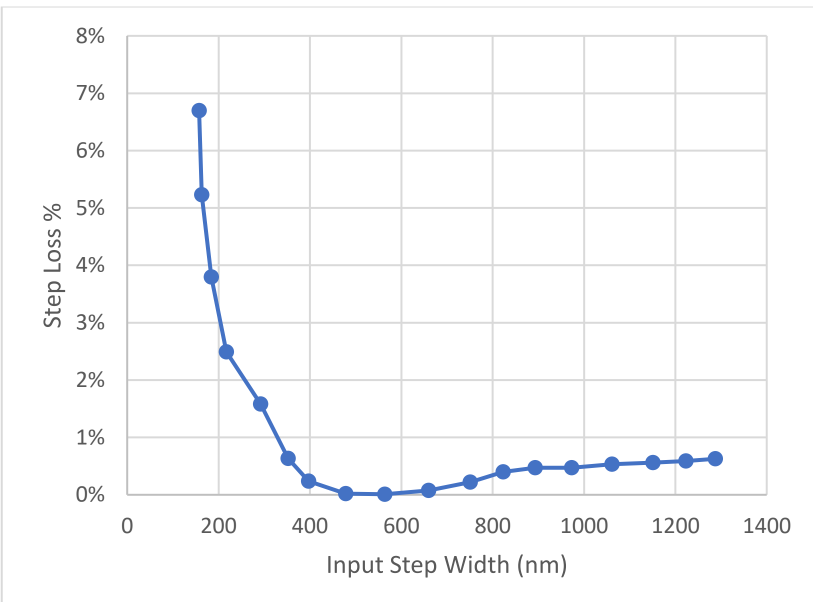

Figure 5 Sample parameter sweeps of step loss as functions of width and change in width. In both examples n_c = 3.44, n_{cl} = 1.5, h= 220 nm. (a) Step loss of waveguide perturbation as a function of step size Input width is 300 nm width. (b) Step loss of waveguide perturbation as a function of initial width.

Note that in Figure 5 (a) the step loss increases monotonically with increasing width perturbation and is convex according to the definition in (Eq. 8). Similarly, Figure 5 (b) shows that the relationship between the step loss and the waveguide width is convex. While the sample curves above are insufficient evidence to claim the CLT is optimal, the surface for $\alpha_{step}\left(w, \frac{\Delta \mathrm{w}}{\Delta \mathrm{z}}\right)$ presented in Appendix A shows the same trends throughout the studied parameter space and therefore provides more convincing evidence of optimality. Still, the argument presented here is not sufficient for a formal proof of convexity and merely suggests that the constant loss taper result may be optimal within the studied interval. A full proof is left to future studies that place the focus more heavily on analytical analysis of mode conversion processes in a nanophotonic waveguide.

It is worth noting that this result in (Eq. 8), which showed that the optimal rectangular waveguide taper profile has constant instantaneous loss throughout, can also be directly applied to slab waveguide tapers or to circular cross-section waveguides by replacing waveguide width with radius in the above discussion. This is consistent with previous studies on tapered waveguides where the optimized profiles in these simple cases were described by Baets to have constant radiation loss throughout [23]. Extrapolating, the constant-loss design principle may be valid for any real waveguide cross-section that depends on one geometric parameter. Furthermore, from a general perspective this discussion demonstrates that functional analysis can be coupled with numerical analysis of large parameter spaces to further understanding of photonic devices.

Constant Loss Taper Calculation Using Coupled Mode Theory

Following the CLT framework in Horth et al., constant loss taper width profiles were derived by discretizing the waveguide taper, as shown in Figure 6, and calculating the coupling coefficient between successive steps. This staircase approximation to tapering waveguide structures has been widely used in the past [8, 21, 29, 39]. After normalizing with respect to power (Eq. 11), we know from coupled mode theory that the coupling coefficient $\eta_{i,i+1}$ is expressed according to (Eq. 12).

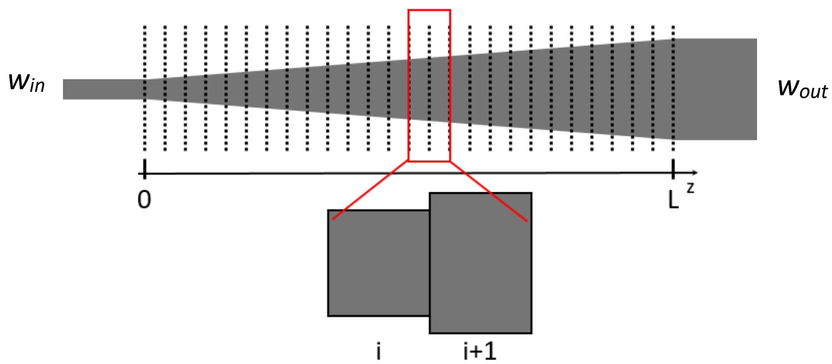

Figure 6 Schematic of discretized inverted taper. Adapted from [8].

$$\int\int E \times H^* \cdot \hat{z} dA = 1 \qquad \text{(Eq. 11)}$$

$$\eta_{i,i+1} = \left|\int\int E_i \times H_{i+1}^*\right|^2 \qquad \text{(Eq. 12)}$$

Using the overlap integral analysis above as an estimate for the transmission from step *i* to *j*, we find the discrete step loss as $\alpha_{i,j} = 1 - \eta_{i,j} - R_{i,j}$, where the step loss refers to the loss incurred at a step discontinuity in the width of the waveguide. The reflection at each step is assumed to be very small and therefore the approximation that $R_{i,j} = \left|\frac{\Delta(n_{eff})_{i,j}}{\sum_i^j n_{eff}}\right|$ is used. This is valid unless a large target $\alpha_{i,j}$ is chosen, which results in a large change in width. In this case, the algorithm generates large $\Delta\left(n_{eff}\right)_{i.j}$ steps, resulting in significant reflections. Thus, an upper limit is present on the choice of $\alpha_{i,j}$. Otherwise, note that the choice of a discrete target step loss has no effect other than to dilate or contract the CLT shape. This is shown below in Figure 7, where the calculated constant-loss taper width profiles as a function of normalized step number are presented for different choices of the discrete step loss $\alpha_{i,j}$. Here the step losses for each curve correspond to attenuations of 0.12%, 0.15%, and 0.18% per step. These are reasonable targets for the step loss as they are small enough to be associated with a small perturbation in the waveguide width, and therefore reflections are negligible. However, they are still large enough that numerical error does not play a significant role in the optimization.

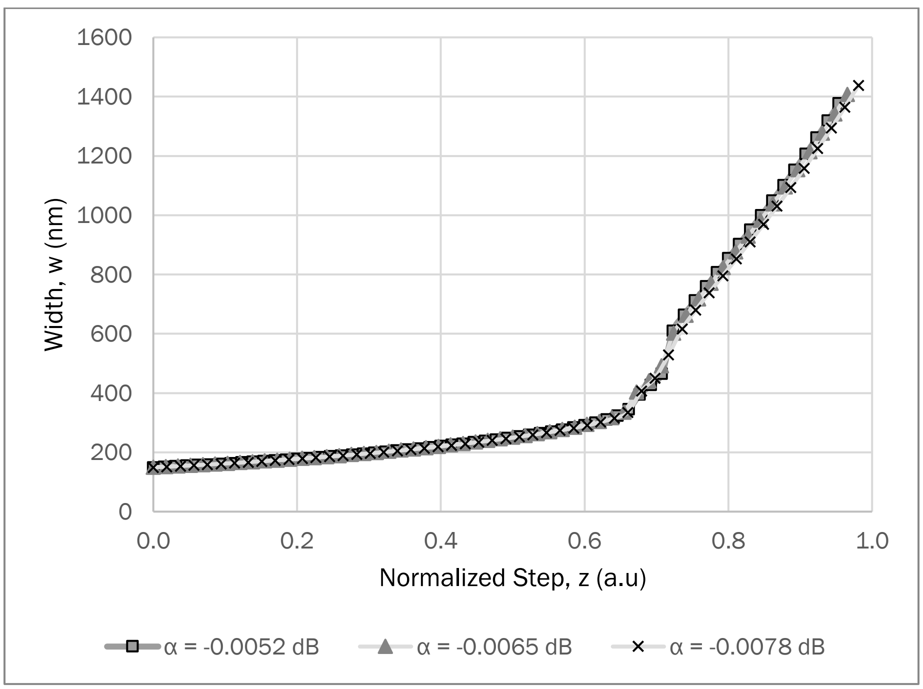

Figure 7 Effect of discrete target step loss in dB on derived CLT profile between a width of 100 and 400 nm.

As the modeling approach based on modal overlap integrals assumes that there are no losses within the waveguide steps, see the diagram of discretized taper in Figure 6, the model does not describe the effect of the inverted taper length on coupling losses. Instead, it serves only to describe how relative losses change with the inverted taper geometry under adiabatic conditions. This fact allows the results in Figure 7 to be scaled to the same curve. In practice, the length of the inverted taper will influence the total performance. Also, the model assumes an infinite cladding surrounding the strip waveguide. For small waveguide widths, the size of the cladding may constitute an additional source of error. Other sources of error, such as leakage to the substrate would also affect the taper performance and result in deviation from the model's predictions.

To calculate guided modes at each step in the discretized taper, a two-dimensional, full-vectorial, frequency-domain, finite-element model was constructed in GNU Octave, as described in [46]. Octave is a free to use programming language that is syntax compatible with MATLAB and largely sponsored by the Free Software Foundation [47]. To ensure the accuracy of the modes generated by the frequency domain solver, a cell size of 0.2 nm was used within the waveguide core. A stretched mesh was also used in the cladding region to decrease the overall resolution and thereby reduce the computational load. Similarly, symmetry boundary conditions were used to limit computation cost. For quasi-TE modes, E_y was set to zero in the *x*-dimension boundary condition, and for quasi-TM modes, E_y was set to zero in the *y*-dimension boundary condition. A typical magnetic field component is presented below in Figure 8 for a 200 nm x 300 nm waveguide. In this mode profile we see that there is significant energy present in the cladding, which requires a large simulation region on the order of 1 μm^2. This requirement increases exponentially with decreasing waveguide size. As a result, simulations of the tip of the inverted taper can be very memory intensive.

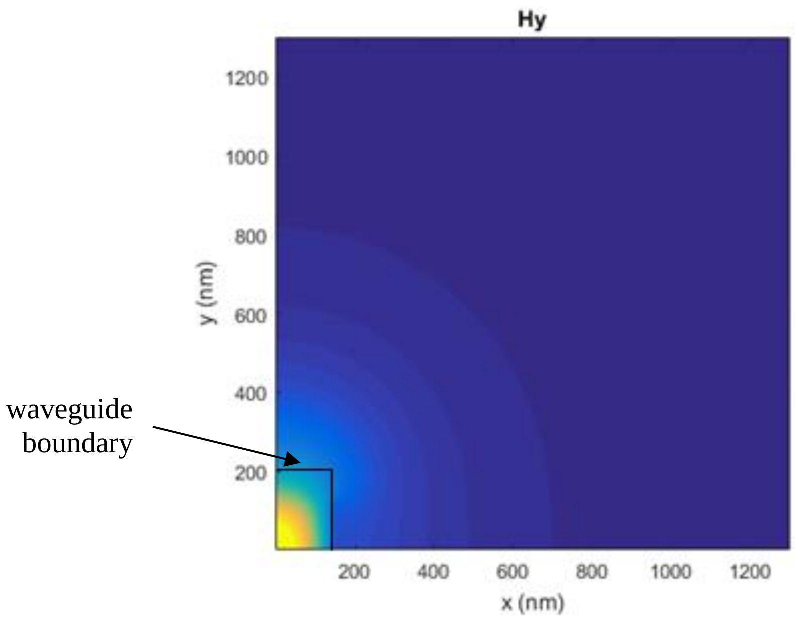

Figure 8 Sample H_y component of a 1550 nm mode resulting from a full-vectorial finite element calculation of a silicon waveguide embedded in a silica cladding for a waveguide height of 200 nm and a width of 300 nm.

This solver was used at each step in the discretized taper to first calculate the local fundamental TE mode, and then find the width of the following step required to the constant step loss target (α). The width perturbation was optimized through a simple bisection method algorithm to achieve this target loss. As this optimization problem was convex with a single turning point, the bisection algorithm was guaranteed to find the width perturbation that provided a target loss, within some tolerance. The analysis was performed for waveguides up until a final width of 1500 nm, which is well above 400 nm, the typical waveguide width in practical applications.

Previously, Horth et al. implemented a similar modeling approach to produce inverted CLT couplers that had the highest efficiency per length ratios reported to date [8]. However, Horth presented a CLT profile for a single set of parameters. Therefore, implementation of a CLT in another context would require repeating the optimization procedure, a process that is time consuming and resource intensive. To enable the widespread use of CLTs, the dependence of constant loss taper profiles on the waveguide height and choice of optical materials was investigated in this thesis. As this requires running many iterations of the above procedure, the complete method for deriving the constant loss taper in Octave and Python was parallelized using the standard Message Passing Interface (MPI), allowing it to be run iteratively on the Guillimin high-performance computing cluster, which is managed by the McGill center for High Performance Computing (HPC). As we shall see below, this large-scale parallelized simulation led to empirical equations describing optimal inverted taper structures for typical applications. These may be used to generate taper width profiles for any waveguide platform after performing a single parameter sweep to find the effective refractive index as a function of waveguide width.

Results

Using the methodology outlined above, a collection of CLTs were generated for different refractive index contrasts, rectangular cross-sections, and target taper losses. This investigation was limited to the 1.55 μm wavelength, which is most commonly used in optical communication networks. However, the inverted taper is well known to have broadband performance and the findings here could be used for nearby wavelengths with little expected impact on overall performance or optimality.

The general shape of the CLT width profile was presented in Figure 7 in the previous section and is reproduced for a single loss parameter as the green curve in Figure 9 below. Here, a rectangular inverted taper SOI waveguide with a 150 nm tip width and 220 nm height is presented. The width is plotted against the normalized step number instead of the integer step number because the derived taper geometry is not dependent on the number of segments in the discretized taper.

For a taper with a given total loss, we have found the same geometry is derived so long as the step number is large enough that the step loss is small, on the order of -0.006 dB.

General trends in Figure 9 are related to the scaling behavior of the effective mode area with waveguide dimension in Figure 3, which is correlated to the effective refractive index. At very narrow widths, the spatial spread of the guided mode is most sensitive to changes in the taper dimension and therefore the width changes slowly. In this region, for normalized step between 0 and 0.5 in the example below, the mode resides primarily outside the core, so the effective index is near that of the cladding. As the waveguide width continues to increase, the guided mode is increasingly confined to the waveguide core and modal area begins to stabilize. A greater rate of tapering is then required to achieve the target constant loss. Eventually a turning point, labeled $z*$ in Figure 9, is reached where the modes resides almost entirely in the waveguide core. This point coincides with the minimum of the effective mode area in Figure 3. At $w*$, the width associated with the turning point, the step loss is the least sensitive to width perturbations. This fact can be demonstrated by plotting the calculated step loss as function of the instantaneous width and change in width. Shown in Appendix A (b), this surface has a clear peak at $w*$, where the system is virtually lossless for small changes in width. The effective mode area will increase with increasing width beyond $w*$. In this regime, very rapid waveguide tapering is required to maintain constant loss as $\frac{\partial EMA}{\partial w}$ is significantly lower than prior to the turning point, see Figure 3.

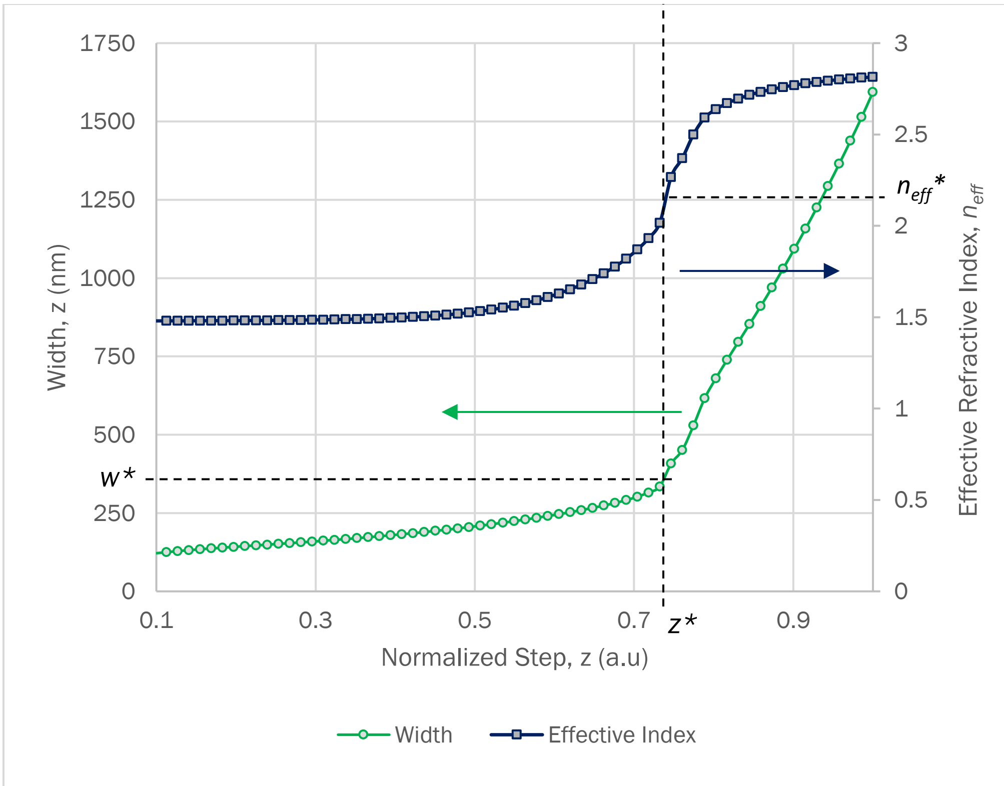

Figure 9 Example CLT width and effective index profiles with $n_c = 3.48$, $n_{cl} = 1.48$, h= 220 nm

Rather than studying width profiles, a preferred method of studying inverted CLT structures is to investigate their effective refractive index profiles. The effective refractive index is a dimensionless parameter and therefore allows for improved comparison of different waveguiding systems. More importantly, it is inversely proportional to the phase velocity, which is closely related to the mode field diameter and waveguiding structure. This makes it a good descriptor of the mode conversion process that occurs in the inverted taper coupler. Overall, these characteristics make the effective index inherently more suitable as a fitting parameter than the waveguiding width.

In the effective index profile in Figure 9, we see that the effective index follows a sigmoid-like function with position, starting at the cladding refractive index and approaching the effective index of an equivalent slab waveguide. As was the case for the EMA plot in Figure 3, two distinct regimes divided by the critical width, $w*$, can be identified. These will be herein referred to as the cladding dominated regime ($w \leq w^*$) and the core dominated regime ($w > w^*$), since the cladding index dominates behavior in the first case while the properties of the waveguide core dominate in the second case. Note that the effective index profile exhibits an inflection point at the critical width. In the core dominated regime, the taper width expansion is roughly linear and therefore relatively easy to model. However, the form of the taper in the cladding dominated regime is less straightforward. Fitting CLT profiles in these two regimes for different parameters will be discussed in more detail in the following sections.

Qualitative Trends

Integrated waveguides are widely studied in the silicon on insulator (SOI) material system, and the constant loss inverted taper was initially developed for this use case [8]. However, CLT geometries will change depending upon the choice of materials. Furthermore, with the advent of metamaterial waveguides and photonic crystals, any number of refractive index systems could be used in an inverted taper. To better understand the relationship between material properties and optimized taper profiles, the effect of cladding and core refractive indices was studied for common material systems. The cladding refractive index was modeled between $n_{c\ell ad}$ = 1.6, which would correspond to a high index glass or polymer, and $n_{c\ell ad}$ = 1.0, the refractive index of air. Meanwhile, the core refractive index was varied from n_{core} = 3.0, just below that of phosphide materials such as InP and GaP at a wavelength of 1.55 µm [48], to n_{core} = 3.6, which is just above the refractive index of doped silicon [49]. In addition, different waveguide heights are used for integrated circuits depending upon the application. To understand the influence of the waveguide height on the constant loss taper, waveguide heights between 200 nm and 300 nm were simulated. As we shall see in the following two sub-sections, the CLT retained a sigmoid-like effective index distribution over the three dimensional (n_{clad}, n_{core}, h) parameter space of interest.

Effect of Material System

Two CLT effective index profiles are compared in Figure 10 (a) for different cladding indices. Here the inverted CLT has a tip with of 150 nm and is calculated to a final width of 1500 nm. The plots show that, holding the core index constant, raising the cladding index does not change the CLT profile significantly in the core-dominated regime. This is because the fundamental guided mode at the beginning of the inverted taper, where the waveguide is narrow, is quite diffused and resides primarily in the cladding. Meanwhile the guided mode at later stages of the taper resides mostly in the core region. The small effect seen in this plot in the core-dominate regime is due to exponential tail regions of the guided mode profile that reside in the cladding. Overall, changing the cladding index simply results in a shift in the constant loss taper's initial value of the effective refractive index.

Similarly, the effect of changing the refractive index of the waveguide core primarily affects the core-dominated region of the CLT effective index plot, as shown in Figure 10 (b) for core refractive indices of 3.36 and 3.48. The two curves shown in this figure are basically identical up until shortly after the inflection point at $w*$, at which point the effective refractive indices seem to approach limits defined by the index for a slab waveguide. In practice, since the effect of the core index is seen relatively late in the taper, many inverted CLTs will be identical despite having different core materials. For the case plotted in Figure 10 (b), a noticeable difference is only present after an effective index of greater than roughly 2.5 is reached. This corresponds to a waveguide width of around 500 nm when the waveguide's core index is 3.48, and a waveguide width near 700 nm when the core index is 3.36. Many integrated waveguides have dimension smaller than these values, and therefore an inverted constant loss taper coupler would not be affected by varying the core material in these cases.

(a)

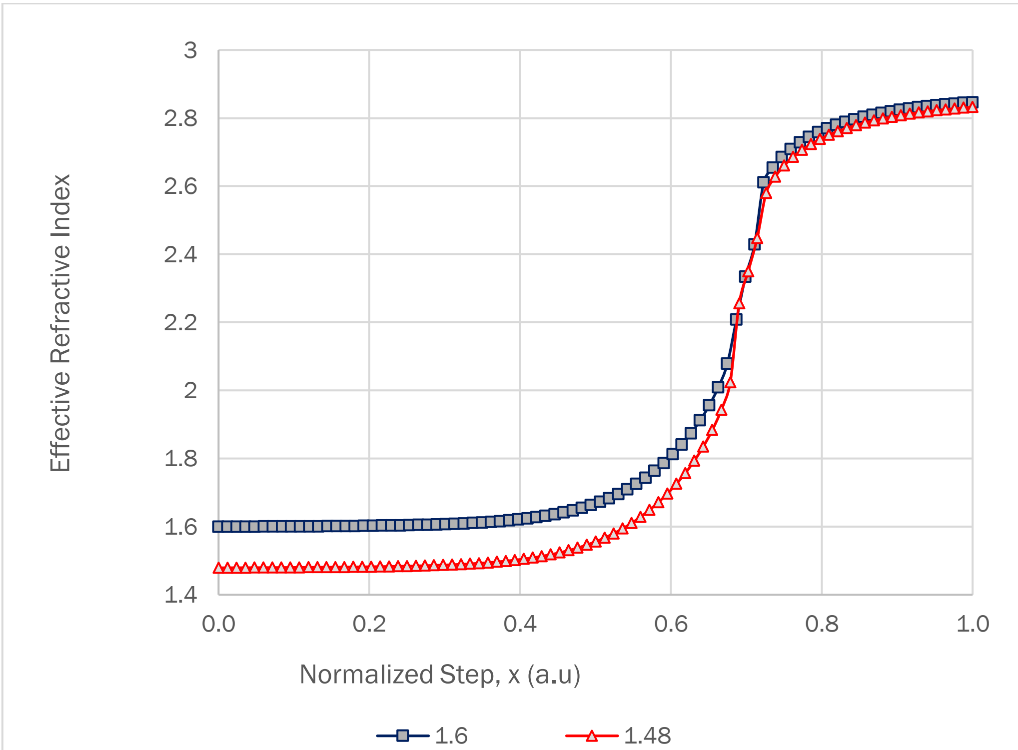

(b)

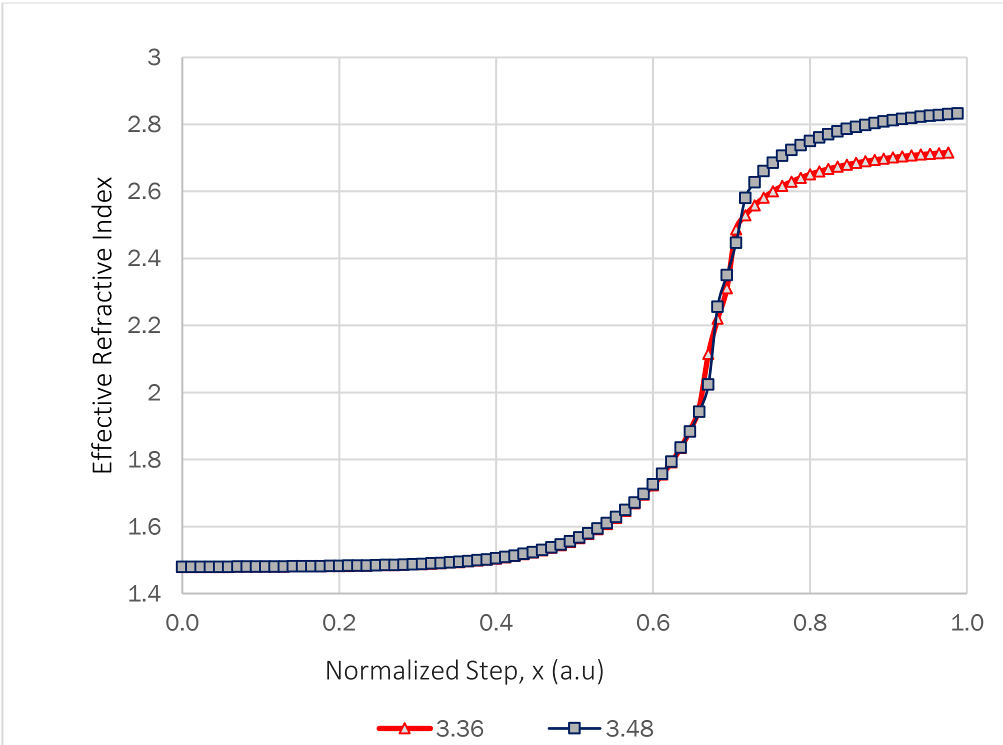

Figure 10 Refractive index on the CLT refractive index profile. In (a) the core index was 3.48 and cladding indices of 1.6 and 1.48 are compared. In (b) the cladding index is 1.48 and core indices of 3.36 and 3.48 are compared. In all cases the waveguides had height of 220 nm.

While the trends shown above are useful for understanding the tapering process, a further simplification can be performed prior to fitting. Namely, we can normalize the effective index according to (Eq.13) to get nearly identical profiles for all cases discussed in Figure 10. This equation simply rescales the effective index profile so that its upper and lower limits, originally equal to the slab waveguide effective refractive index n_{slab} and cladding waveguide index n_{clad}, become 0 and 1. The result of this normalization process is shown in Figure 11, where the normalized effective index ($\hat{n}_{eff}$) curves are presented for the examples shown above.

$$\hat{n}_{eff} = \frac{n_{eff} - n_{clad}}{n_{slab} - n_{clad}} \qquad \text{(Eq.13)}$$

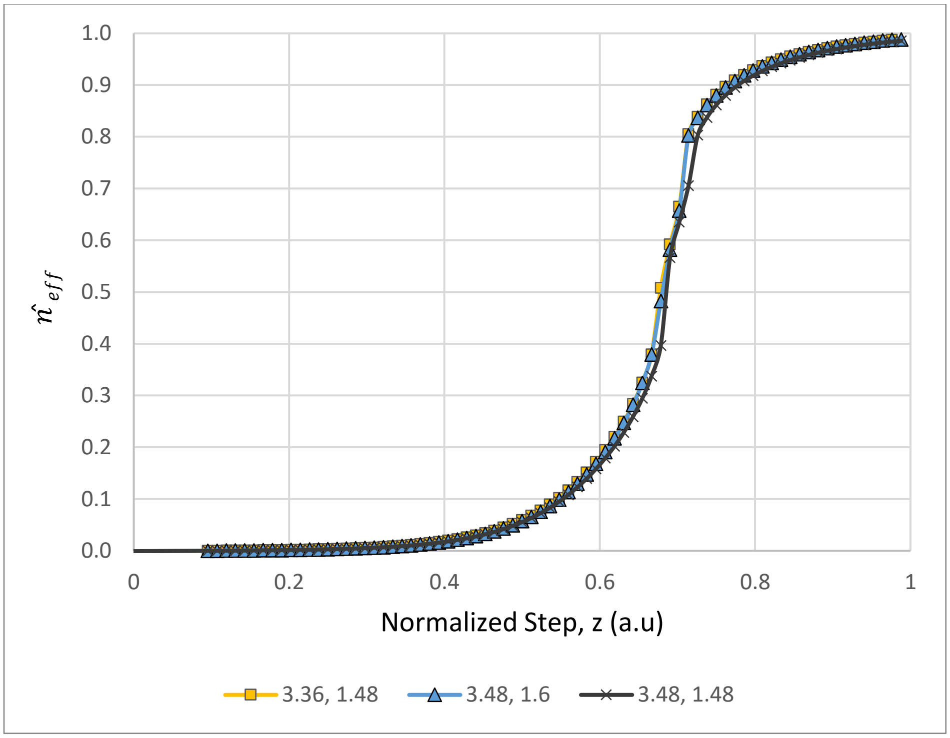

Figure 11 Normalized CLT effective index profiles. Legend labels correspond to waveguide core and cladding indices respectively. Height of waveguide is 220 nm in all cases.

Effect of Strip Waveguide Core Height

In addition to the refractive index of the materials used, the waveguide height strongly affects the CLT effective index profile. This effect is more complicated than that from the waveguide refractive indices. Typical integrated rectangular waveguide heights used in modern application lie between 200 nm and 300 nm, with the most common being the 220 nm SOI platform [14]. Heights larger than 300 nm are challenging to fabricate with narrow tip widths in the inverted taper application, and heights smaller than 200 nm exhibit less confinement, and are therefore less common.

Effective refractive index profiles are shown for waveguides with heights of 220 nm and 300 nm in Figure 12 (a). There are two important differences between the presented curves. First, there is a change in the inflection point that demarcates the boundary between the cladding and core dominated regions. Increasing the height results in a leftward shift of the inflection point as the taller waveguide will confine the guided mode within the core at a smaller width. Second, there is a change in the curvature of the effective index profile. A clear decrease in the slope is seen at the inflection point when the waveguide height is increased from 200 nm to 300 nm. This trend can again be explained as resulting from the higher effective refractive index of the structure when the height of the waveguide core is increased at a fixed waveguide width. The change in curvature is seen more clearly in Figure 12 (b), where instead of plotting against the step number normalized to the total step number, we have normalized the *z* axis such that both curves exhibit the same inflection point at *z'* = 0.5. We will herein refer to this normalized coordinate as *z'*. Rescaling the *z* axis does not impact the physical geometry represented by the inverted taper profile as length is not considered in our discretized taper model. As we shall see, expressing the curves in new coordinates such as *z'* will be useful for fitting.

(a)

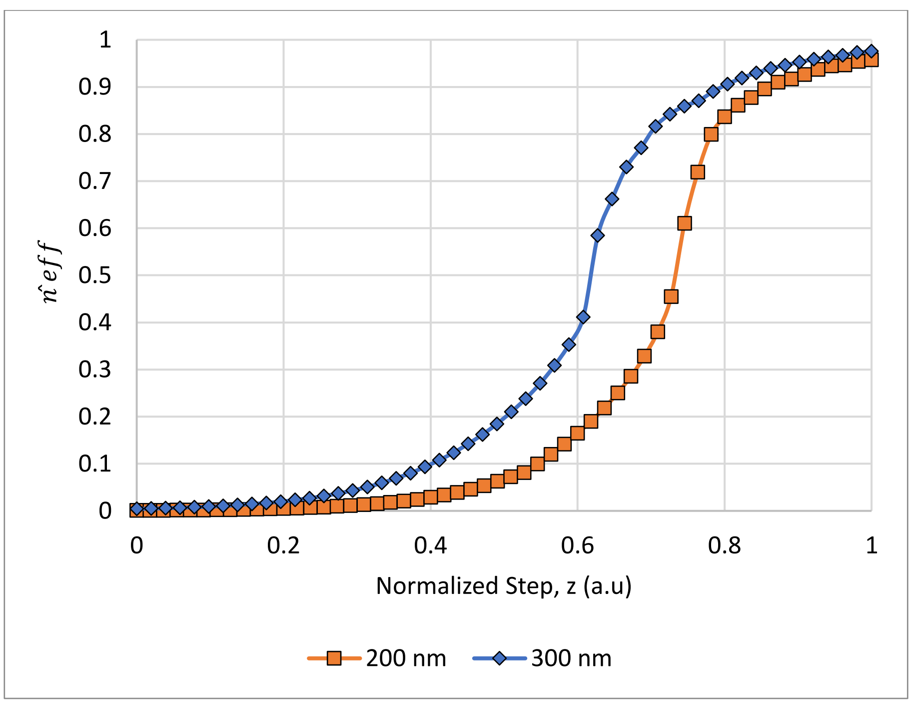

(b)

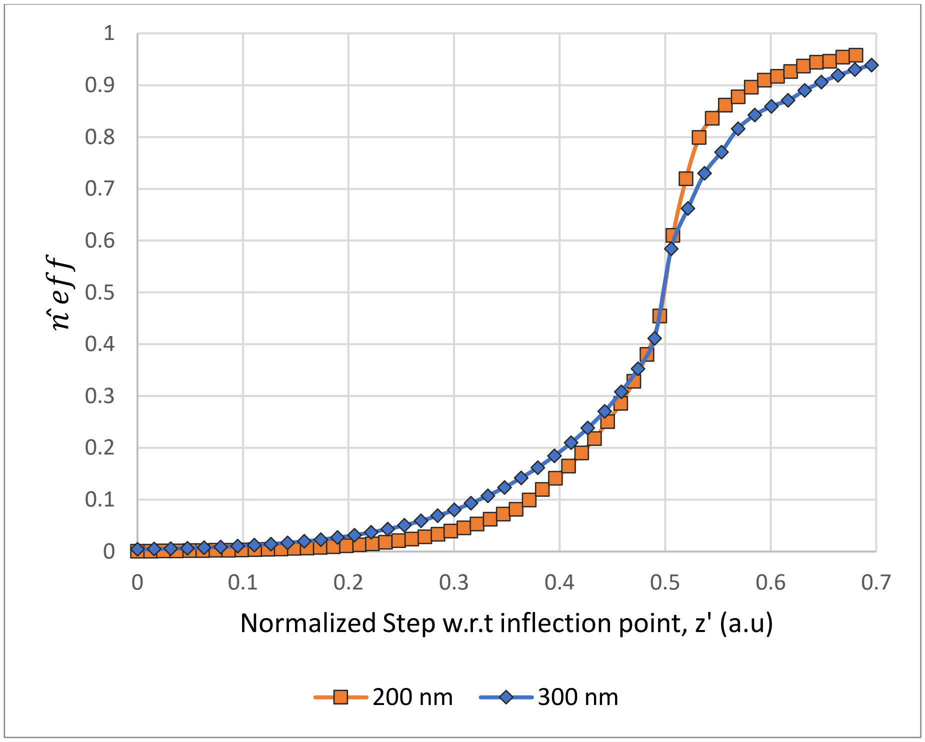

Figure 12 Effect of waveguide height in nanometers on CLT refractive index profile. (a) position normalized to final width, (b) normalized to inflection point. Waveguide core has index 3.48 and cladding has index 1.48.

Parametric Fitting of Constant-Loss Taper Effective Index Profiles

The collection of parameter trends discussed above can be summarized in two equations for the normalized effective index profile in constant-loss tapers. For all CLTs derived in this paper, the $\hat{n}_{eff}$ profile initially followed an exponential increase. However, as the width of the taper continues to increase with propagation distance, the taper's effective refractive index must approach a limit that represents the refractive index of a slab waveguide, which has infinite width. Unfortunately, the asymmetry of the derived CLT effective index profiles made it difficult to fit with a single logistic or alternative sigmoid function. As a result, the fitting function proposed here is piecewise, containing an exponential function for the cladding-dominated regime and a rational function for the core-dominated regime. This equation is presented in (Eqs.14) alongside a typical fit in Figure 13. This is an approximate function that will work well for empirical fitting and for examining trends in the CLT profiles over the parameter space.

$$\hat{n}_{eff}(z') = \frac{n_{eff,\ CLT} - n_{clad}}{n_{slab} - n_{clad}} = \begin{cases} \frac{1}{2} e^{-k_{clad}(z'-1/2)}, & z' < 1/2 \\ \dfrac{1}{1 + \dfrac{1}{k_{core}\left(z' - \frac{1}{2}\right) + 1}}, & z' \geq 1/2 \end{cases} \quad \text{(Eqs.14)}$$

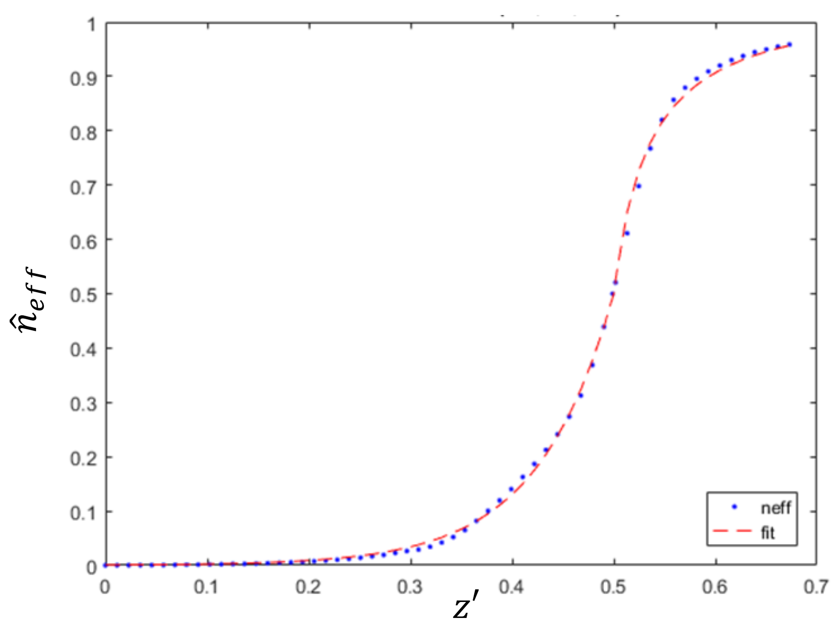

Figure 13 Fitting curve for n_{clad} = 1.5, n_{core} = 3.44, and height = 220 nm

As was the case previously, z' is the normalized step along the discretized taper in arbitrary units such that the point z' = 0.5 demarcates the cladding and core dominated regions. The refractive index n_{slab} in (Eqs.14) represents the effective index of a slab waveguide with the same height, cladding, and material properties as the tapering structure. Finally, k_{clad} and k_{core} are dimensionless fitting parameters that were found for each CLT in the parameter sweep.

The fitting procedure first rescaled the raw data such that z' = 0.5 at the inflection point and z' = 0 at the start of the taper. Next n_{slab} was found analytically from a slab waveguide model. With this information, it was possible to normalize the effective refractive index as shown in (Eq.13) and perform linear regressions to find k_{clad} and k_{core} in (Eqs.14) for each CLT effective index profile. The k_{clad} and k_{core} fitting procedure was performed on the McGill HPC Guillimin following the previously mentioned CLT geometry computational process.

Surfaces for k_{clad} and k_{core} as a function of n_{clad}, n_{core} and waveguide height were generated by running the simulation and fitting procedure for many waveguide systems. These surfaces were then fitted via a multilinear regression to establish a fully empirical description of the CLT geometry's parameter dependence. The resulting goodness of fit plots are shown in Figure 14, where the predicted coefficients $\hat{k}_{clad}$ and $\hat{k}_{core}$ are plotted against the real values k_{clad} and k_{core}. The full regression results with coefficients are shown in Appendix B. Here the multilinear regression for k_{clad} had an R^2 of 0.93, while that for k_{core} was lower at 0.76. The lower R^2 for k_{core}, the parameter that defines the curve in the core dominated region, may be due to there being fewer data points in this part of the effective index curve. That is, the fitting process is more prone to error since there are fewer points and a greater proportion of points in the set lie near the inflection point. This region is also the least stable in the optimization because the shape of the CLT is derived sequentially, starting with the tip, which results in greater accumulated error in the later part of the reported curves.

(a) (b)

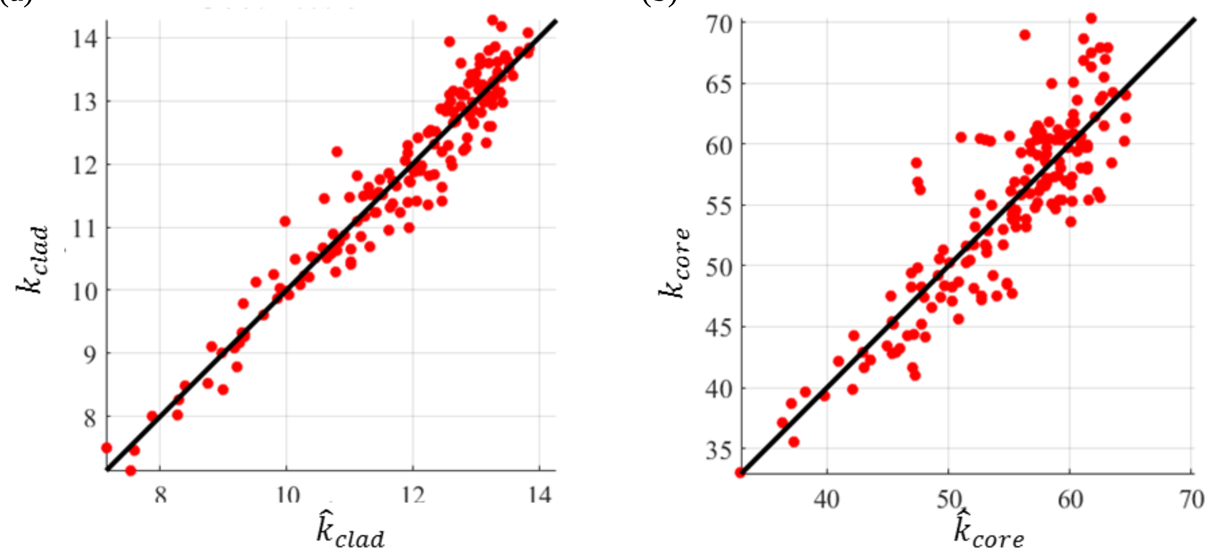

Figure 14 Goodness of fit curves for multilinear regression of (a) k_{clad} and (b) k_{core}.

Despite the somewhat lower R^2 value for k_{core}, the fitted polynomial surface represents the data well and can provide us with some insight into the mode conversion process in inverted constant loss tapers. Also recall that the core dominated region is less important to practical inverted taper design as it usually applies to waveguide widths in the multi-mode regime that are larger than those commonly used. Figure 15 shows the fitting parameter values for constant height as a function of the refractive index of the core and cladding materials. Figure 16 plots the values of the fitting parameters for constant cladding refractive index, but varies the height and core refractive index. In these figures we see that the surfaces for k_{clad} and k_{core} are similar. This is because they both relate to the curvature of the effective refractive index profile. For example, in Figure 12 (b), the profile for a 200 nm waveguide height has a greater curvature than that with a 300 nm height, and this is reflected in the fact that the 200 nm height inverted taper has a normalized effective index profile with larger k_{clad} and k_{core} than that for the 300 nm height inverted taper.

Near the center of the studied parameter space, the k_{clad} and k_{core} surfaces have a very small gradient, meaning that the normalized effective index plots (e.g. Figures 11 or 12b) are nearly the same, as was seen qualitatively earlier. However, as we approach extremes in the refractive index (e.g. n_{core} = 3.6, n_{clad} = 1.6), the fitting parameters begin to change. A rough trend is that greater values for k_{clad} and k_{core} are seen when the waveguide structure has an intrinsically low effective refractive index, and therefore greater phase velocity. The constant height contour surfaces in Figure 15 and the constant cladding index surface in Figure 16 illustrate this finding. This is particularly evident in the latter case (Figure 16) where we see that increasing the core index decreases the fitting coefficient values. The same trend is also present in Figure 16 for increasing waveguide height: Larger heights result in greater mode confinement and decreased phase velocity, which translates to smaller k_{clad} and k_{core} that reflect decreased growth rates for the normalized effective refractive index profiles.

(a)

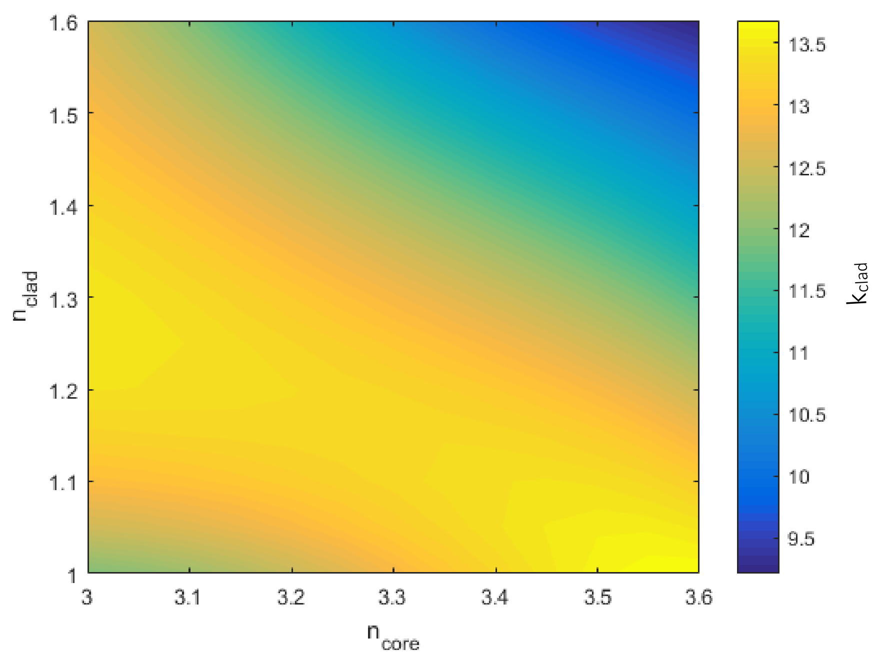

(b)

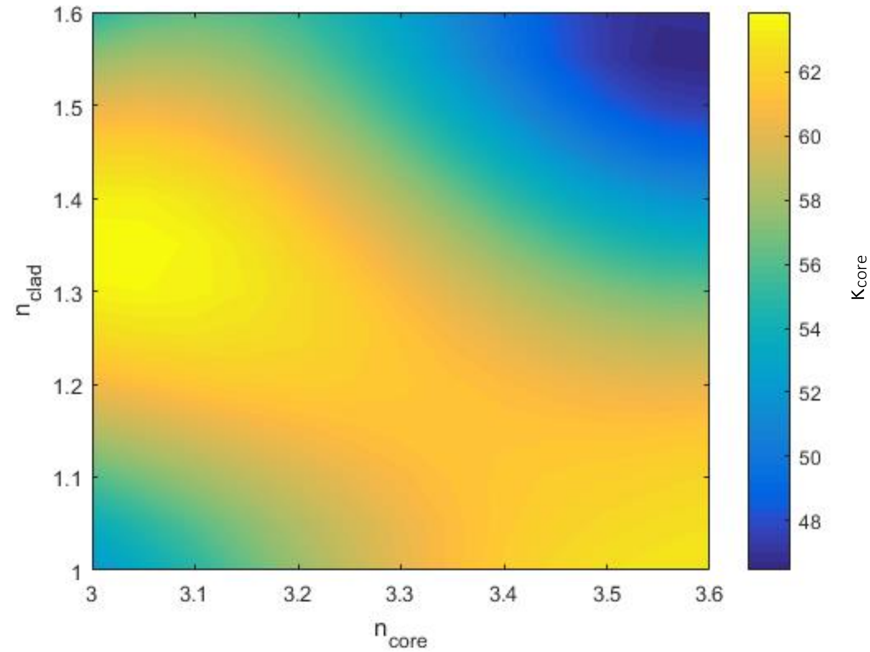

Figure 15 Surfaces for (a) k_{clad}, (b) k_{core} in the n_c – n_{cl} space for constant height of 220 nm.

(a)

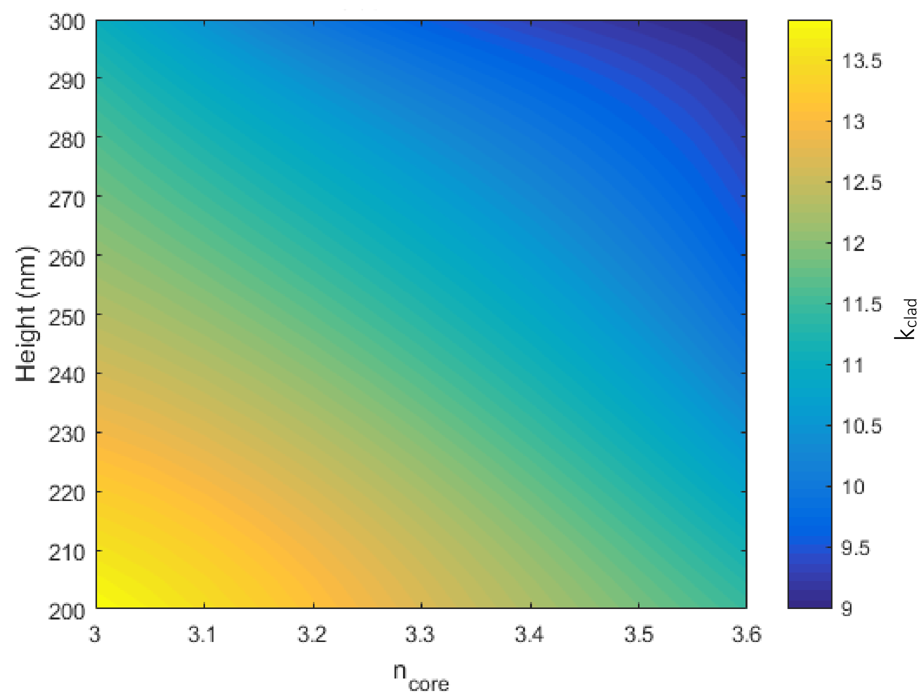

(b)

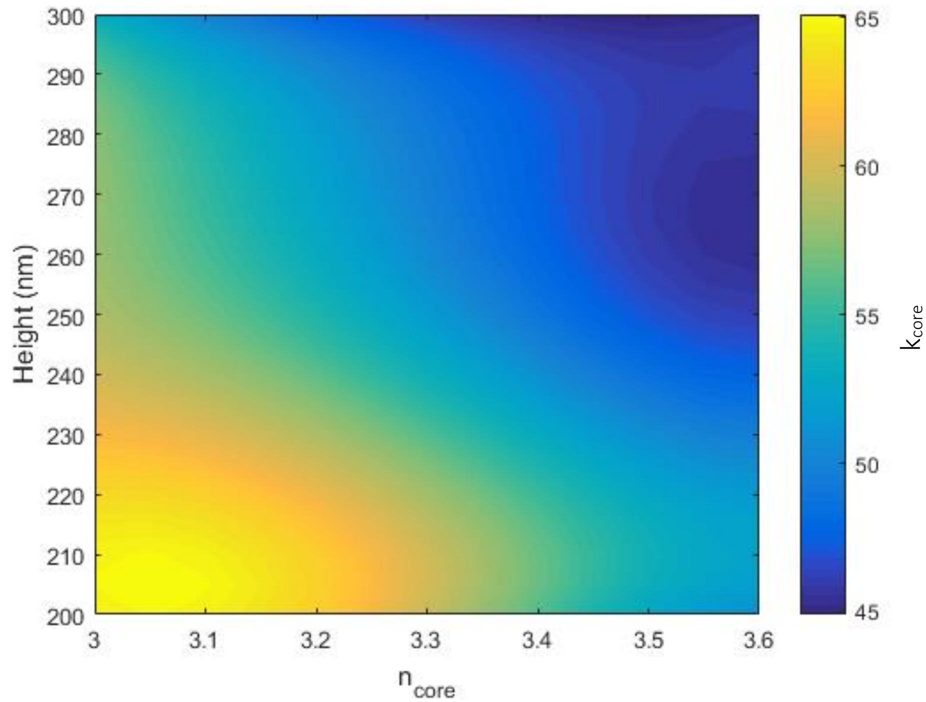

Figure 16 Surfaces for (a) k_{ckad}, (b) k_{core} in the n_c – h space for cladding index of 1.40.

The close correlation between the trends in the fitting parameters and the intrinsic waveguide effective index is show more explicitly in Figure 17 (a) and (b), where the effective index of a waveguide with width of 400 nm is plotted over the refractive index and height parameter space. These two surfaces seem inversely correlated to those presented above for the fitting parameters This suggests that differences in k_{clad} and k_{core}, and therefore the CLT geometries, may be a result of our *z'* axis scaling. To clarify, in our fitting procedure the starting point was a tip width of 150 nm. However, systems with larger waveguide height or refractive index contrast have greater normalized effective refractive indices at this initial width. This increased starting point results in smaller values for k_{clad} and k_{core}. By eliminating this effect, we shall see that a global curve is found that describes all constant loss taper geometries. This is done by rescaling the *z'* axis such that all curves begin at the same normalized effective index value.

(a)

(b)

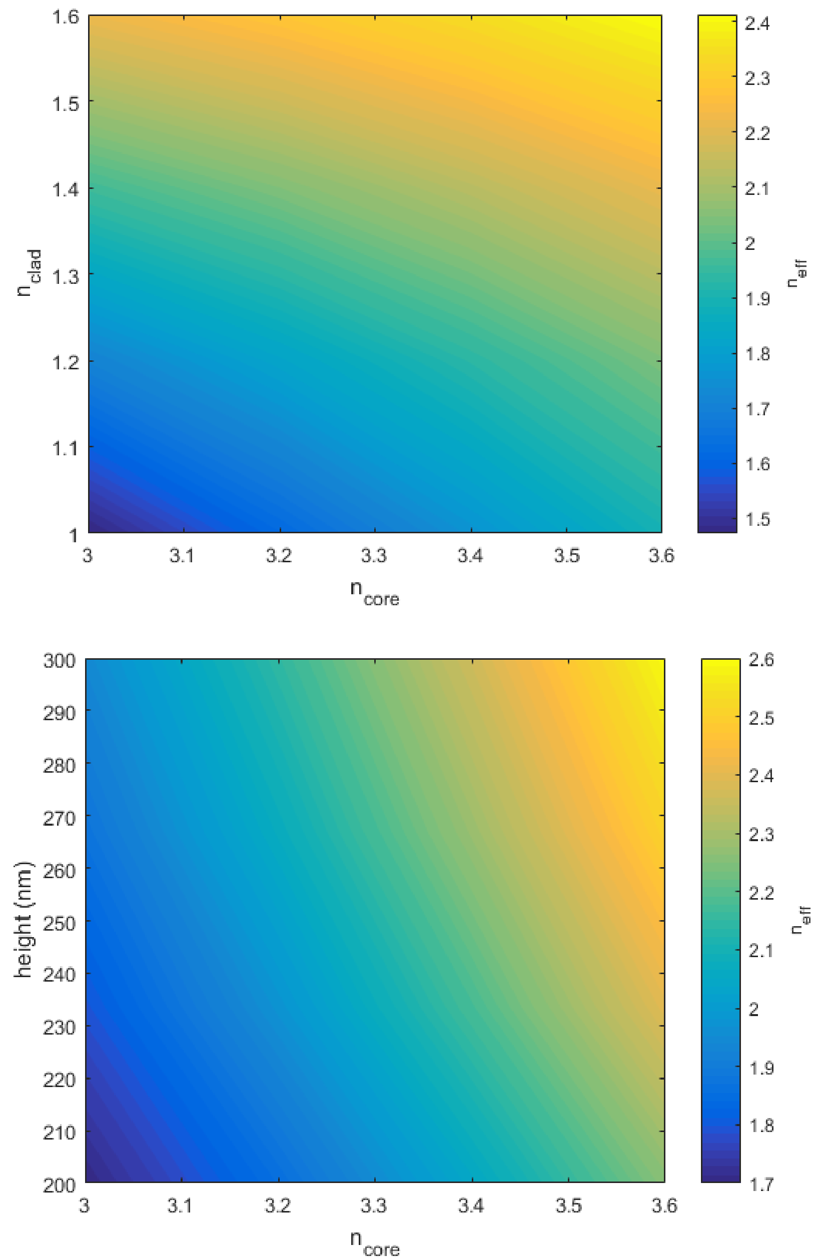

Figure 17 Surface for effective refractive index of a 400 nm x 220 nm waveguide as a function of (a) the core refractive index and cladding refractive index and (b) the core refractive index and the waveguide height.

Following the result discussed above, the normalized effective index profiles in terms of z' were rescaled such that they each began with a common starting $\hat{n}_{eff,initial}$. We refer to this rescaled coordinate as x. The $\hat{n}_{eff}(x)$ data after this rescaling procedure are shown in in Figure 18 as a scatter plot. We see that there is a very limited difference in the profiles over the entire parameter space. In fact, the variations in the normalized index profiles are likely within simulation errors resulting from uncertainties in the effective index calculation and overlap integral method of calculating the step loss (Eq. 12). The implication of this result is that a single global normalized-effective-index curve could be used when designing a constant loss inverted taper regardless of the application specific material system or waveguide platform. This global or average curve is presented in Figure 18 as a dashed black line. The fitting parameters for the global normalized index profile are k_{clad} = 12.18 and k_{core} = 42.60.

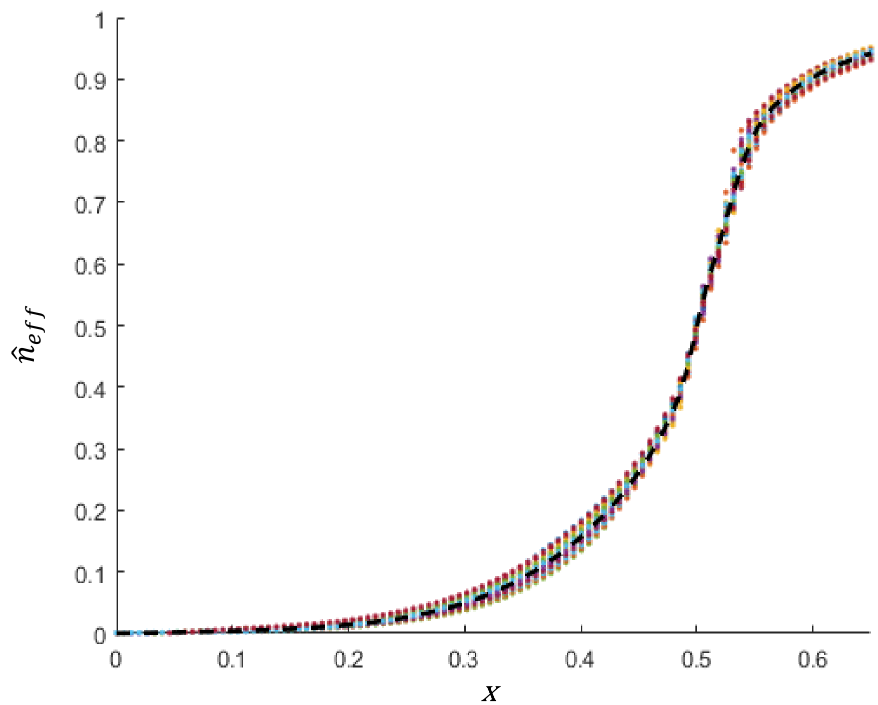

Figure 18 Global normalized effective index curve plotted alongside scatter data of 25 randomly selected rescaled CLT $\hat{n}_{eff}(x)$ profiles.

Finding Constant Loss Taper Geometry from the Global Normalized Effective Index Curve

The discussion above has identified that inverted nanophotonic tapers share a common normalized effective refractive index profile. However, what is most important from a practical perspective is not just the existence of a global normalized effective index profile, but rather the taper geometry and performance that are generated from the profile. In general, we have found that width profiles back-calculated form the global normalized effective index curve match very well with the raw constant loss width profiles derived numerically in this study.

If the relationship between fabrication parameters, design parameters, and material choices is well understood for a given waveguiding system, then it is very simple to calculate the taper geometry associated with the global normalized effective index profile. To find the width profiles from the global normalized effective index profile, the effective index profile for the system of interest is first found by mapping the global, normalized-effective-index profile to the interval (n_{clad}, n_{slab}). Then, a parameter sweep of the waveguide width is performed to find n_{eff} as a function of the waveguide width. The width profile of interest can then be interpolated from this curve. Note that to implement this approach in practice the effective index of the waveguide system must be very well understood.

Figure 19 (a) – (d) plots four constant loss inverted taper width profiles calculated from the global effective index curve alongside the raw width profiles derived from our simulation for three different cases. Figure 19 (a) – (c) show the results for elevated cladding refractive index, waveguide height, and core refractive index respectively, and Figure 19 (d) shows a standard case where n_{clad}= 1.4, n_{core} = 3.4, and h = 240 nm. In each case the difference between the width profiles back calculated from the global normalized effective index curve and the raw data is within around ten nanometers. This is a relatively small error, on the order of fabrication error in many cases. The global effective-index profile therefore seems to be a reliable and simple method of designing an inverted CLT, which is quicker and more simple to implement than running a custom electromagnetic optimization procedure.

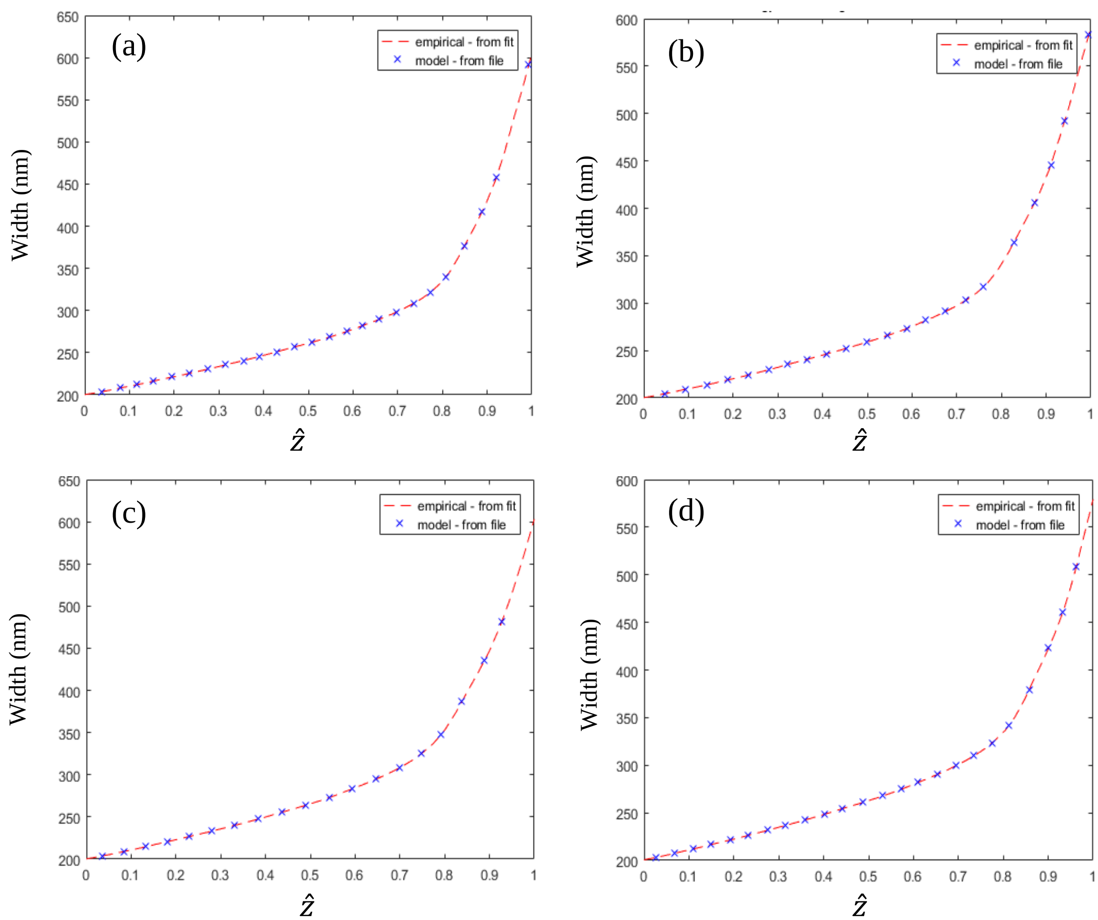

Figure 19 Comparison of width profiles calculated from global $\hat{n}_{eff}$ empirical curve with those found from numerical model for (a) n_{cl} = 1.4, n_c = 3.6, h = 200 nm, (b) n_{cl} = 1.4, n_c = 3.4, h = 280 nm, (c) n_{cl} = 1.6, n_c = 3.4, h = 240 nm, (d) n_{cl} = 1.4, n_c = 3.4, h = 240 nm.

Having established that the global effective index profile is indeed capable to reproducing the raw numerical results with sufficient accuracy, the question of relative performance should be addressed. In terms of performance, we can compare the relative losses of the calculated constant loss inverted tapers with those of linear inverted tapers. For both families of taper geometries, an inverted taper between 200 nm and 600 nm was divided into 45 segments and the overlap integral method was used to estimate losses. As predicted by the Lagrangian analysis of the waveguide tapering problem, significant loss improvement is seen throughout the parameter space, for all studied cases. This is illustrated in Figure 20 (a) – (c), which show the ratio of the loss in the CLT to the loss in the linear taper for constant cladding refractive index, core refractive index, and waveguide height respectively. When light is guided primarily in the cladding-dominated regime, as was the case for the waveguides studies in this example, the core index does not significantly affect the relative performance of the CLT. This is reflected in the horizontal and vertical contour lines in Figures 20 (a) and (b) respectively. From these figures, it is also clear that the benefits of the CLT are accentuated at lower waveguide heights and at smaller index contrasts, or more generally when the waveguide system is less confining. This trend is easily explained as there is more mode conversion taking place between the input and output widths under these conditions. The initial mode at the tip of the inverted taper is more diffused when the core is less substantial (has smaller refractive index or decreased height), and the optimal mode conversion approach yields greater benefit as a result.

From these surfaces it can therefore be concluded that the underlying theory regarding the optimality of the constant loss taper is correct for at least the parameter space studied here. The design of optimal inverted taper geometries can thus be greatly accelerated by using the global normalized effective index curve.

(a)

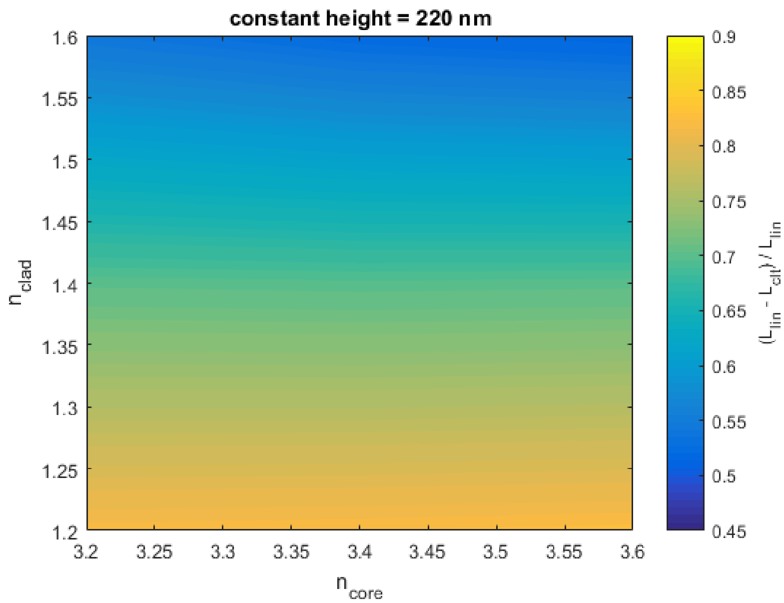
constant height = 220 nm
1.6
1.55
1.5
1.45
1.4
1.35
1.3
1.25
1.2
n_{clad}
3.2
3.25
3.3
3.35
3.4
3.45
3.5
3.55
3.6
n_{core}
0.9
0.85
0.8
0.75
0.7
0.65
0.6
0.55
0.5
0.45
$(L_{lin} - L_{clt}) / L_{lin}$

(b)

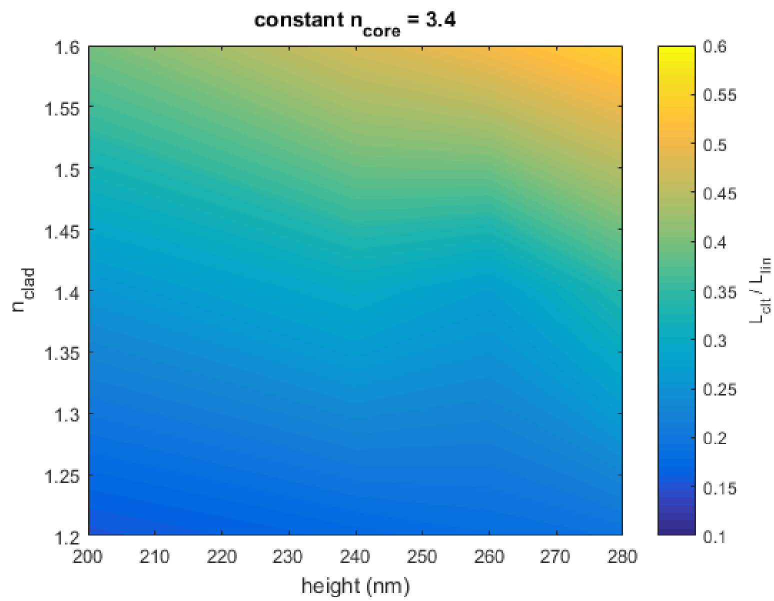
constant n_{core} = 3.4
1.6
1.55
1.5
1.45
1.4
1.35
1.3
1.25
1.2
n_{clad}
200
210
220
230
240
250
260
270
280
height (nm)
0.6
0.55
0.5
0.45
0.4
0.35
0.3
0.25
0.2
0.15
0.1
L_{clt} / L_{lin}

(c)

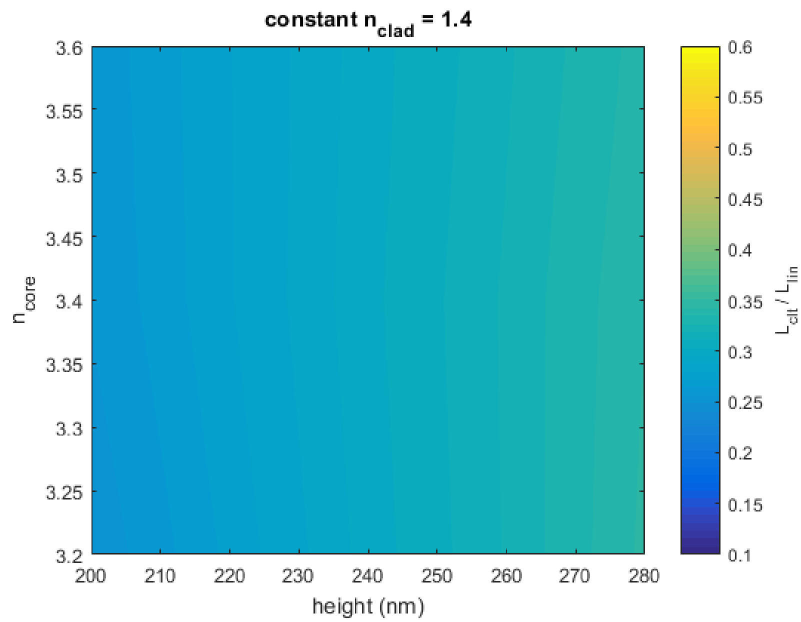

Figure 20 CLT loss relative to a linear taper loss between a 200 nm and a 600 nm strip waveguide for the studied parameter space. (a) constant height, (b) constant cladding index, (c) constant core index. All units of height are in nanometers. The plotted value is ratio: $\frac{L_{CLT}}{L_{linear}}$.

Summary

Coupling between fiber optics and integrated waveguides is an important problem faced whenever photonic components are implemented in our modern communications networks. Among the many methods for converting optical modes present in fibers to those present in nanoscale waveguides, the inverted taper coupler proves one of the most promising due to its high efficiency, relatively small footprint, and broadband performance. Several principles exist in the literature for the design of tapered waveguides. Unfortunately, they are generally hard to apply in modern applications as they were either not developed for three dimensional waveguides or are overly qualitative.

The constant loss approach to inverted taper coupler design appears to be an exception. This Lagrangian approach arises from analyzing the mode conversion process in an adiabatic inverted taper coupler through the lens of functional analysis. In this paper, we have examined the geometry of constant loss inverted tapers by leveraging high performance computing and parallelized simulations with the goal of furthering our understanding of these structures and finding methods to simplify their design. This analysis led to the development of a new framework for describing the inverted taper mode conversion process, which focused primarily on the study of the normalized effective refractive index ($\hat{n}_{eff}$) profile along the propagation direction of the inverted taper. This normalized effective index was found to be a valuable descriptor of the mode conversion process in fiber-to-chip couplers because it is dimensionless and closely, though not directly, related to the spatial spread of the guided mode.

The $\hat{n}_{eff}$ profile followed an asymmetrical, sigmoid-like shape along the constant loss taper, with an inflection point at the critical waveguiding dimension (w*) where the effective mode area was minimized. This critical turning point separates two regimes of waveguide tapering: the cladding-dominated regime, where the mode phase velocity is primarily a function of the cladding refractive index, and the core-dominated regime where, as the name suggests, the core refractive index is of most importance. In the cladding-dominated regime an exponential form for the normalized effective index $\hat{n}_{eff}$ was found, which is likely related to the exponential increase in the effective mode area with decreasing waveguide dimension (see literature review discussion). Meanwhile an algebraic function best fit the change in the effective index in the core-dominated regime. The difference in functional form may be the result of inherently different mode conversion processes taking place in the two regimes. The cladding-dominated regime exhibits rapid mode contraction with increasing width, while the core-dominated regime exhibits slow mode expansion. The asymmetry of the derived profiles in this work is also likely a result of this difference.

Interestingly, the normalized effective index profile along the constant loss taper was nearly the same for the various waveguide systems studied in this thesis when proper normalization was applied. Small differences in the curves for different waveguide heights or materials are attributed to numerical error. The discovery of a single normalized function to describe the constant loss taper allows for a simplified inverted taper coupler design process. First, the $\hat{n}_{eff}$ profile must be found using the reported empirical equations and fitting parameters. The n_{eff} profile can then be found by simply rescaling the $\hat{n}_{eff}$ curve to the interval between the cladding refractive index and the slab waveguide refractive index. Then, the associated waveguide widths can be calculated by performing a single parameter sweep of n_{eff} against waveguide width in any full-vectorial mode solver. The derived map of effective index to width allows the empirical n_{eff} profile to be converted to a width profile which represents the taper geometry. We have performed this process for many waveguiding systems, finding strong correlation between the generated inverted taper geometries and those found from numerical optimization. In addition, it is clear from the results that using a constant loss taper results in significant loss improvements over a linear taper.

Considering the results discussed above, the Lagrangian approach to designing inverted tapers is a promising method for rapidly designing optimal inverted taper structures in fiber-to-chip couplers. In qualitative terms, one can describe the constant-loss approach as simply maximizing the width expansion at each position in the taper without exceeding some tolerable loss. The existence of a common normalized effective index distribution for constant-loss tapers is a result of the fact that we have a good descriptor of the mode conversion process in waveguide tapers, namely the effective index. By normalizing this quantity, we account for the variation in the step loss function with system parameters like the waveguide height and refractive indices. We are thus left with a global trend that describes the constant loss taper expansion. This result is easily applied in practice if the effective index is well known for the material system and structure being used. Therefore, when applying the results of this study to the design of a constant loss inverted taper for any waveguiding system, whether it be a metamaterial, photonic crystal, or wire waveguide, great care must be taken to ensure that the desired effective index is achieved after fabrication.

Looking beyond the empirical equations presented, this study shows that recent growth of computation resources and cloud-based technologies can empower large-scale parameter studies of photonic devices. As was the case here, this expanded computational potential can be enhanced and guided by analytical properties of our parameter spaces. Overall this approach could be adapted to solve many other constrained optimizations problems in photonics.

Chapter 2: Constrained Optimization of Orthogonal Waveguide Couplers with Fixed Footprint

Introduction

Waveguide bends are required components of integrated photonic circuits as they are necessary to maintain compact packaging. They are widely used in devices such as photonic transceivers and receivers, where up to 200 bends can commonly be found [50]. Due to the large number of waveguide bends in integrated photonic circuits, reducing their footprint by decreasing the bending radius can have a significant effect on the size of photonic chips. A similar argument can be made regarding the efficiency of waveguide bends. Reducing the losses in a waveguide bend by a fraction of a percent can hugely impact overall power usage in photonic chips since the total loss is proportional to the loss incurred per waveguide bend to the power of *n*, where *n* is the number of waveguide bends in the device. Unfortunately, the bending radius of a curved waveguide is inversely related to the power coupled into radiation modes. Losses and footprint are therefore two performance metrics that must be balanced in an optimization procedure.

When discussing curved waveguides, often two types of losses are identified: bending losses and transition losses [51]. Bending losses arise from mode distortions that result in radiation of light away from the curved waveguide. They are often modelled as shown in Figure 21, where a radius $R + x_r$ is defined beyond which the wave must propagate above the speed of light to remain in phase. Since this condition cannot be met, the energy associated with the guided field beyond this point is lost by radiation. The critical distance, x_r, can be found in (Eq. 15), where R is the radius, β_z is the propagation constant in the waveguide and $\beta_0$is the unguided light propagation constant [52].

$$x_r = \frac{\beta_z - \beta_0}{\beta_0} R \qquad \text{(Eq. 15)}$$

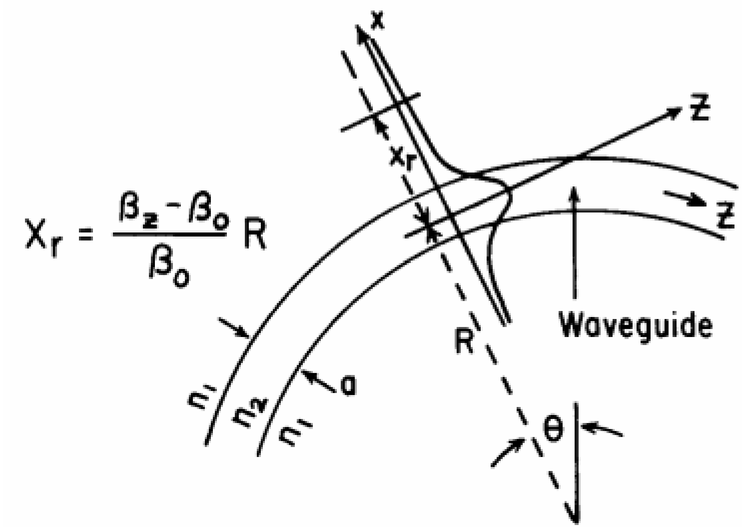

Figure 21 Schematic showing bending loss mechanism in curved waveguide [52]

Meanwhile, the second class of losses in waveguide bends are commonly referred to as transition losses. These are associated with a change in the shape of the guided electromagnetic mode resulting from a change in the waveguide's radius of curvature and are often modeled as the overlap integral of the guided mode within the curved waveguide mode with that present within the straight waveguide [51-54].

As shall be discussed in some detail, many studies have investigated methods of reducing the transition and bending losses in curved waveguides. Approaches have included optimizing the bend geometry [55-57], fabricating trenches [58], controlling the refractive index profile [59], and offsetting the central axis of the waveguide bend from that of the straight bend [60]. However, there has not been a comprehensive study relating the footprint of a waveguide to the optimal bend profile. To further investigate this area, this study will find and analyze the optimal shapes of orthogonal bend waveguides for different footprints through modern full-vectorial finite difference time domain simulations.

Literature Review

Researchers such as Marcuse and Marcatili performed some of the earliest studies investigating bending losses in optical fibers and waveguides [61-64]. Marcatili found an approximate closed-form expression for bending loss in 1969, which he used to identify three guidance regimes for low-index-contrast waveguides [64]. Shortly thereafter, Marcuse published a similar study analyzing asymmetric curved slab waveguides [61, 63]. He would also later compute bending losses via diffraction theory [65]. These early studies found increasingly skewed field distributions within curved waveguides as the radius was decreased, which resulted in an increased imaginary field component in the guided mode and therefore decreased transmission.

In 1975, shortly after these early studies, Heiblum and Harris introduced a conformal transformation to reduce the complexity and computation time associated with modeling curved waveguides [66]. Since then, this approach has been widely used to describe any systems with refractive index gradients [67]. A conformal transformation approach models the curved structure as a straight waveguide by modifying the cross sectional refractive index distribution $\left(n(x)\right)$, which would be a step function for any rectangular waveguide, according to (Eq. 16). Here x represents the distance from the waveguide core in the radial direction, as shown in Figure 21. This approach allows for the guided mode in the bent waveguide to be found by solving the Helmholtz equation under the transformed conditions. Semi-analytical techniques can be leveraged for this task such as the Wentzel–Kramers–Brillouin (WKB) approximation [53, 54, 68] or methods like the one outlined by Lu et al. in 2005 [69]. These techniques have produced more accurate results than simple analytical models for most bent waveguide applications, particularly at smaller length scales.

$$n'(x) = ne^{x/R}$$
$$n'(x) \approx n\left(1 + \frac{x}{R}\right) \qquad \text{(Eq. 16)}$$

The WKB method has been particularly well developed for analysis of bending losses. This technique is widely used in physics to numerically solve linear differential equations. Berglund and Gopinath have performed a complete analysis of bend loss using WKB method with a conformal transformation, finding good correlation between their results and experimental data, as well as the results of more computationally intensive methods of solving this problem [53]. In Figure 22 the conformal transformation of the refractive index distribution is shown in the lower subfigure and the associated mode profile found by WKB analysis is shown in the upper subfigure. Here x represents the spatial dimension along the radial direction of the curved waveguide. In the upper subfigure we can see how the guided mode in a waveguide bend is asymmetric, with its peak shifted towards the outer radius of the waveguide. We can also see the cutoff radial position, labeled x_r, beyond which the mode is no longer guided. Note that this results in the presence of an imaginary field component $\mathrm{Im}(E_z)$ which represents the radiation bending losses.

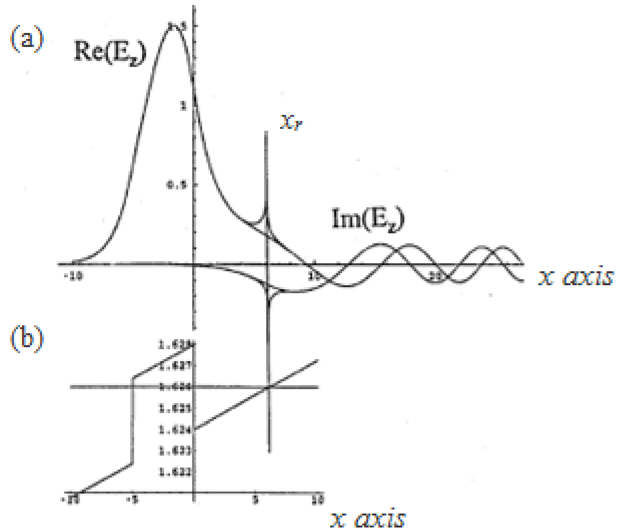

Figure 22 (a) The electric field as a function of radial position *x* (Eq. 16) calculated by WKB approximation for a bent fiber using conformal transformation. (b) The refractive index profile of the wavguide as a function of *x* after applying conformal transformation to the originally rectangular profile [53].

Modal analysis of bent waveguides using the techniques discussed thus far have led to two primary design concepts for reducing losses in curved structures. The first involves offsetting the center of the bent waveguide relative to that of the straight waveguide. This discrete change in the central axes of the straight and curved waveguides serves to maximize the overlap between the symmetric guided mode in the straight waveguide and the skewed mode in the curved waveguide, illustrated in Figure 22. Put forward by Neumann [60], this approach aims to reduce transmission losses. The second approach instead focusses upon reduction of bending losses by increasing the guided mode confinement in the curved region. This has been achieved by either introducing a low index trench in the cladding outside of the waveguide bend, which was also suggested by Neumann [58], or by increasing the width of the curved waveguide region, an idea that has been implemented in several studies [56, 70].

More recently full-vectorial, numerical-propagation-based methods have improved the accuracy of waveguide bend simulations and allowed modeling of 3D waveguides and polarization effects. The need for these simulations arose from inherent limitations in the conformal transformation to describe propagation behavior [71]. Such studies generally used either the finite difference time domain (FDTD) [72], finite element method (FEM) [71], or beam propagation method (BPM) [73]. The BPM calculates solutions to the Hemholtz equation for a curved waveguide using a Fast Fourier Transform (FFT), which makes it very computationally efficient. Studies such as Schermer and Cole (2007), have successfully used the BPM to predict bending losses in single mode and multimode fibers [73]. Despite the fundamentally different approach taken, the authors noted that their numerical simulation results matched well experimental results and those found numerically using techniques outlined by researchers such as Marcuse [74]. This similarity can be seen in Figure 23 from their paper which plots the bend loss against bend radius.

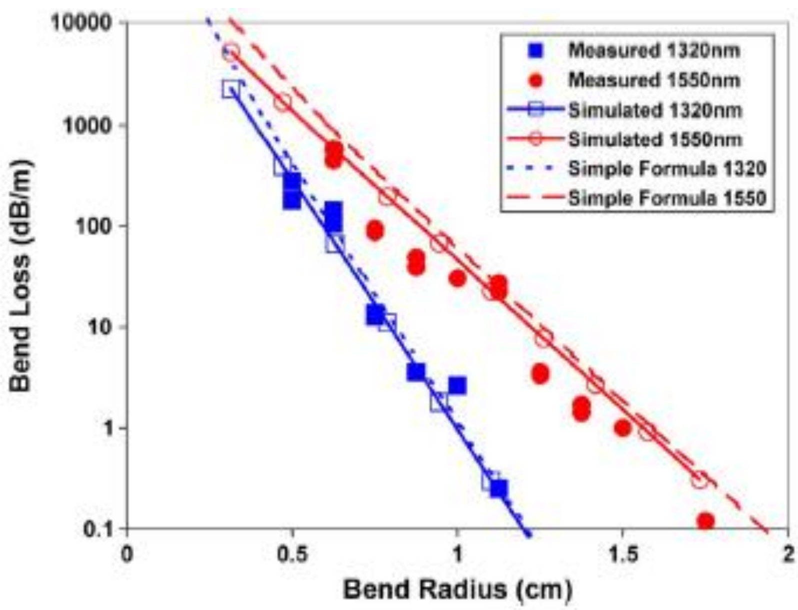

Figure 23 Comparison of bend loss vs bend radius for an SMF-28 fiber using BPM simulation with other techniques from Schermer et al. at 1550 and 1320 nm [73]

Likewise, FDTD and FEM simulations of curved waveguides have been successfully performed in the past, though many of these have focused on designing photonic crystals to reduce losses and dispersion [75, 76]. In the past, FDTD simulations of nonlinear waveguides faced issues surrounding boundary conditions and computational time. However, these obstacles can be overcome by using a perfectly matched layer (PML) boundary conditions to improve the accuracy of FDTD models [77]. Studies by Wu et al. [78] and other research groups [79-81] have further developed the method in FDTD such that it is now commonly used to analyze a wide range of photonic systems including those containing curved waveguides. Similar developments have been made by Coccioli et al. [82] and Jedidi et al. for the finite element method [83, 84]. Curved waveguide FDTD studies such as those by Yuan in 2008 [85] and Wang in 2010 [86] have shown similar trends as those reported by Marcuse [65], as shown in Figure 24. These curves, which show the scaling behavior of losses with bending radius, will have a critical role in interpreting the optimization results.

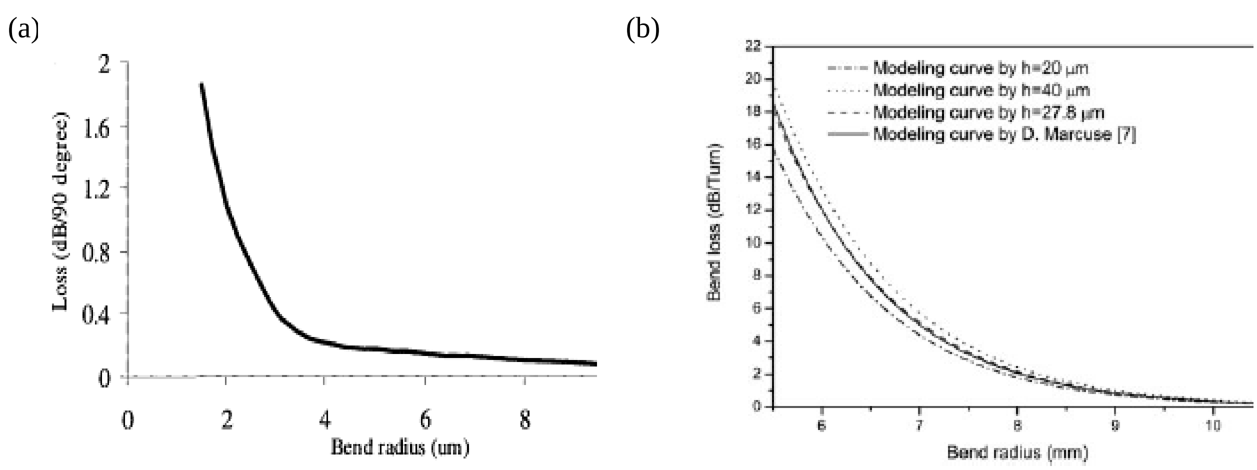

Figure 24 Bending loss versus radius for 90º bends of a submicron waveguide using FDTD. (a) Result from Yuan using 500 nm wide waveguide and λ=780 nm (b) Comparison between Wang [86] and Marcuse [65] for SMF28 fiber of different radii at λ=1550 nm. Fiber has silica core and fluorine doped cladding. [85]

Many optimization studies have been published that leverage the above numerical methods. Early in the 1990s, Smit et al. [70] optimized the curved waveguide width and offset using modal analysis and Yamauchi, et al. [87] performed optimization studies of trench parameters for a slab waveguide. A few years later a more relevant trench analysis for 3D waveguides was presented by Seo et al. using a semi-vectorial, finite-difference analysis [88]. More recently, finite difference optimization of different bend structures has been published by Anderson et al. [89] and Harjanne et al. [90], looking at slot waveguides and ridge waveguides respectively. Several papers have also been reported where genetic algorithms or particle swarms were implemented for curved waveguide optimization. Coccioli [91] and Khanzadeh [55] were two such studies that used the finite element method. Unfortunately, many of these studies report on narrow parameter spaces, focusing on methods rather than results. Single use cases are often analyzed and reported geometries are therefore not easily adapted to practical contexts. In addition, there seems to be no definitive answer as to what functional form is optimal for the bent waveguide.

In summary, previous studies investigating the effect of curvature on wave propagation have used a wide range of techniques to perform their analysis. Analytical methods have been employed with success in 2D waveguide bend simulations, and numerical methods including the WKB approximation [53], FDTD [72, 75, 81, 86], and BPM [73, 92] have also proved reliable in the past for simulating these structures in 2D and 3D. However, there has not yet been a definitive conclusion on the optimal shape of a 90^{o} bent waveguide, or a topological analysis of how these shapes scale with footprint. In this thesis chapter, we will attempt to fill this gap in knowledge by optimizing a typical integrated silicon waveguide bend for a range of different footprints, investigating scaling laws and bending parameter surfaces in the process.

Modeling

Finite difference time domain modeling has been used intensively since the 1990s to model wave propagation in optical devices. The method involves meshing the geometry of interest and solving Maxwell's equations as finite difference equations with spatial and temporal dimensions. Lumerical, a commercial FDTD software, was used in this study to model orthogonal rectangular silicon waveguide bends for device footprints between 1 μm^2 and 100 μm^2. Here the footprint was defined as the area of the smallest square that could contain the waveguide bend. For a circular bend, the footprint would be equal to the square of the bend radius plus the half the waveguide width. Perfectly matched layer (PML) boundary conditions and a spatial buffer of greater than one micron between the simulation boundaries and the waveguide were used to prevent simulation artifacts, such as reflection off the boundary or errors in the fundamental guided mode calculation. A 1550 nm fundamental TE mode source was injected to the bend and mode expansion monitors were placed at the input and output of the bend to sample the guided mode. An example simulation setup is presented in Figure 25, which was created in the Lumerical user interface [93]. Here the blue region represents the integrated waveguide, the yellow lines are power monitors, the pink arrow shows the propagation direction of the injected mode, and the borders represent the PML region.

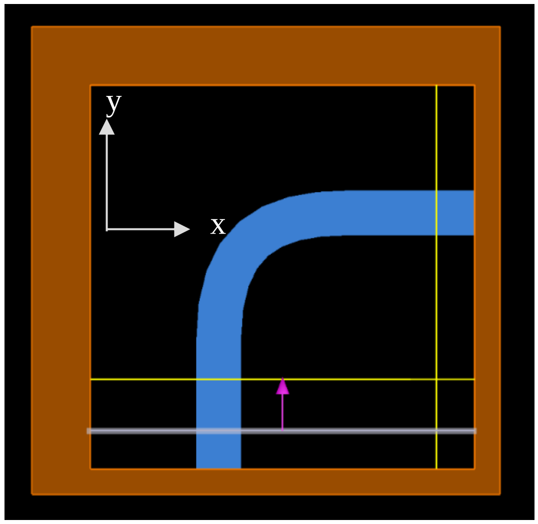

Figure 25 Typical waveguide bend simulation setup.

The waveguide bend shape was described by a Bezier curve with four control points and the exact waveguide path was derived from (Eq. 17). Bezier curves are parametric curves representing piecewise polynomials that can be used to approximate a wide range of bends. Here the typical Bezier curve notation is used where n represents the number of control points, $\mathbf{P}_i$ represents the i-th control point, and u represents the position along the bend. The shape of the curve is represented by $\mathbf{C}(u)$. The coordinates of the curve at position u along the bend is found by taking the sum of control points weighted by the factor $B_{n,i}(u)$, which can qualitatively be interpreted as representing the contribution of a given control point to the local bend shape.

$$\mathbf{C}(u) = \sum_{i=0}^{n} B_{n,i}(u)\mathbf{P}_i$$
$$B_{n,i}(u) = \frac{n!}{i!\,(n-i)!} u^i (1-u)^{n-i} \qquad \text{(Eq. 17)}$$

The local derivative of a Bezier curve can then be found according to (Eq. 18). For our application, the initial and final derivative must be continuous with the input and output orthogonal waveguides. This condition fixed the first and final control points, as well as one of the coordinates of each of the remaining control points. Therefore, two independent parameters remain to define the shape of a given coupler profile, which are the y coordinate of $\mathbf{P}_1$ and the x coordinate of $\mathbf{P}_2$. Under the symmetry condition, a relationship can be derived between the two central control points, namely they take the form in (Eq. 19). Here we have designated the y-coordinate of the $\mathbf{P}_1$ control point a. For a circle, the value of a is roughly equal to 0.552. Diagrams showing the construction of asymmetric and symmetric Bezier curve are shown in Figure 26 (a) and Figure 26 (b). The dotted lines between control points are related to the derivative of the Bezier curve as shown in the equations below (Eq. 18).

$$\begin{gathered}\frac{d}{du}\mathbf{C}(u) = \sum_{i=0}^{n-1} B_{n-1,i}(u)[n(\mathbf{P}_{i+1} - \mathbf{P}_{\mathrm{i}})] \\ \frac{d}{du}\mathbf{C}(0) = n(\mathbf{P}_1 - \mathbf{P}_0), \qquad \frac{d}{du}\mathbf{C}(1) = n(\mathbf{P}_n - \mathbf{P}_{\mathrm{n}-1})\end{gathered} \tag{Eq. 18}$$

$$\begin{gathered}\mathbf{P}_1 = (0, a)^{\mathrm{T}} \\ \mathbf{P}_2 = (1 - a, 1)^{\mathrm{T}}\end{gathered} \tag{Eq. 19}$$

(a)

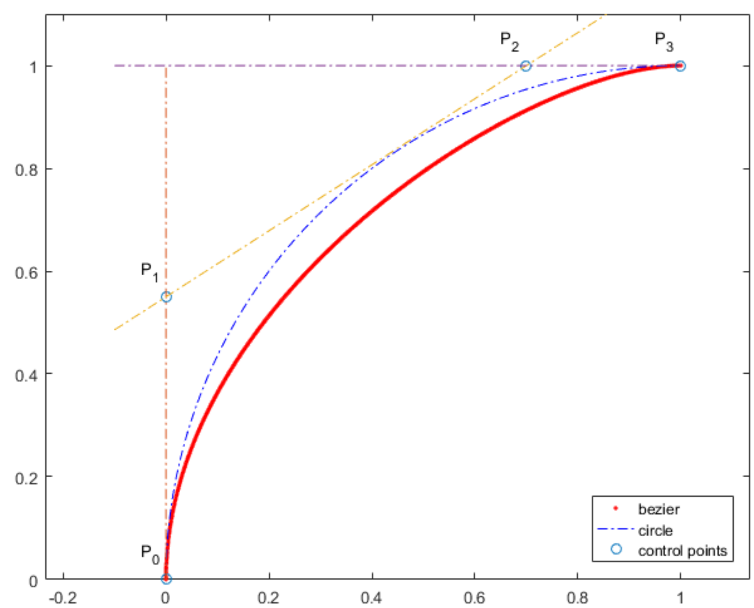

(b)

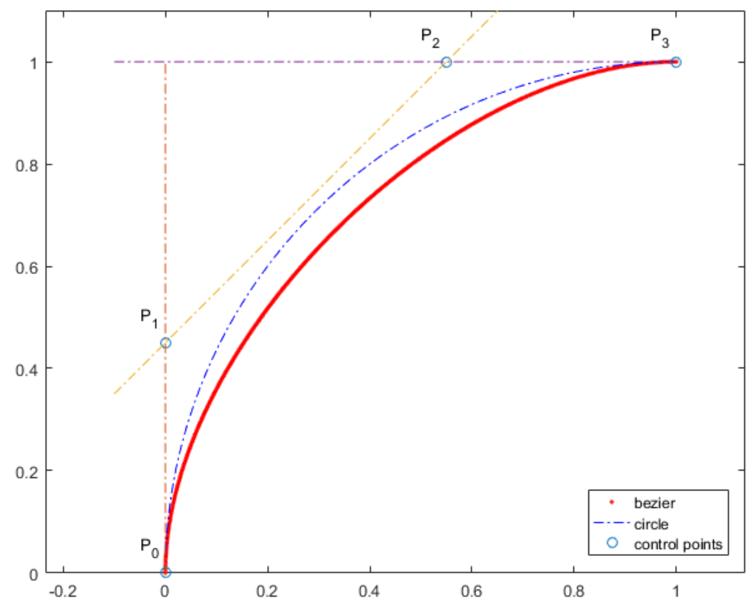

Figure 26 Diagrams of Bezier curve construction for (a) asymmetric curve with P1 = (0, 0.55), P2 = (0.7, 1) and (b) symmetric curve with *a* = 0.4. Note that units here are normalized to unity.

When the waveguide bend was assumed to be symmetric according to (Eq. 18), the rate of convergence was increased by an order of magnitude. It is clear this symmetry condition is valid if the waveguide bend should operate for modes injected from both directions. In addition, a symmetric solution may be optimal in some cases when only one propagation direction is required due to the underlying loss mechanisms. For example, consider the limit case where transmission losses dominate. Since transmission losses calculated by overlap integrals are agnostic to propagation direction, there is no benefit to having asymmetric transmission losses at the input and output facet when in the absence of bending losses. A similar argument could be made for bending loss limit case as it is not clear how the transmission would improve with an asymmetric path. For any skewed distribution of curvature along the bend, the same performance should be achievable with a symmetric distribution. In a skewed curvature distribution, bending losses would simply be spread asymmetrically along the waveguide bend, while the opposite would be true in the symmetric case.

However, when transmission and bending losses are comparable an asymmetric structure could yield improvements. In this case, as bending losses attenuate the guided power through the waveguide, the absolute transmission loss resulting from a curvature change at the end of the 90^o bend would be smaller in absolute terms than the absolute transmission loss resulting from the same curvature change at the start of the waveguide. Therefore, an overall improvement would be achieved by strategically placing higher changes in curvature towards the end of the waveguide bend. For simplicity, symmetric structures will first be investigated in the discussion that follows. Asymmetric solutions will then be studied to test the reasoning outlined here.

Whether waveguide bend symmetry was imposed or not, a particle swarm optimization procedure was implemented to search for the control points that define the path of lowest loss between the two orthogonal waveguides. This technique involved running several hill-climbing optimizations in parallel that were seeded at different starting points. High performing optimization threads are given computational priority over those that found themselves in sub-optimal locations. After each iteration of the optimization procedure, the calculated fields were analyzed in MATLAB. The objective function for the optimization calculated the overlap integral of the mode captured by the final monitor, which was located in the output orthogonal waveguide, and the fundamental guided mode of the linear structure. This overlap integral for total transmission *T* is shown in (Eq.20), where E_o, H_o are the output fields, and E_f, H_f are the calculated fundamental modes.

$$T = \frac{\left|\int\int E_o \times H_f^*\right|^2}{\left|\int\int E_o \times H_o^*\right| \cdot \left|\int\int E_f \times H_f^*\right|} \qquad \text{(Eq.20)}$$

Results

The path connecting two orthogonal waveguides was optimized to maximize transmission for various device footprints using a particle swarm optimization of 3D FDTD simulations. In this section we will first discuss the optimization results found by assuming a symmetric solution to the orthogonal coupling problem. Afterwards the validity of this assumption will be tested by considering the larger asymmetric parameter space. All results reported below were generated by modeling the propagation of the fundamental TE mode at 1550 nm through 90^{o} bends of 350-nm-wide silicon strip waveguides with silica cladding. Figure 27 (a) and (b) show typical optimized 90^{o} waveguide bends alongside reference circular arc for 1 µm^2 and 25 µm^2 footprints. We see that for the 1 µm^2 case in Figure 27 (a), the optimized shape has a decreased path length relative to the arc of a circle (blue). Meanwhile, the optimized Bezier curve path for the larger footprint in Figure 27 (b) has a greater path length.

(a)

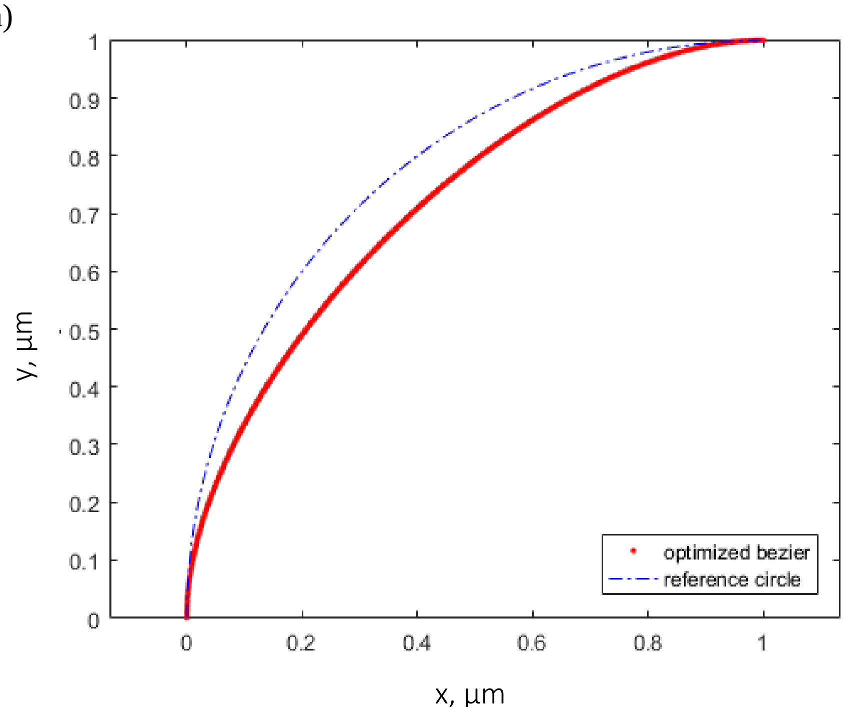

(b)

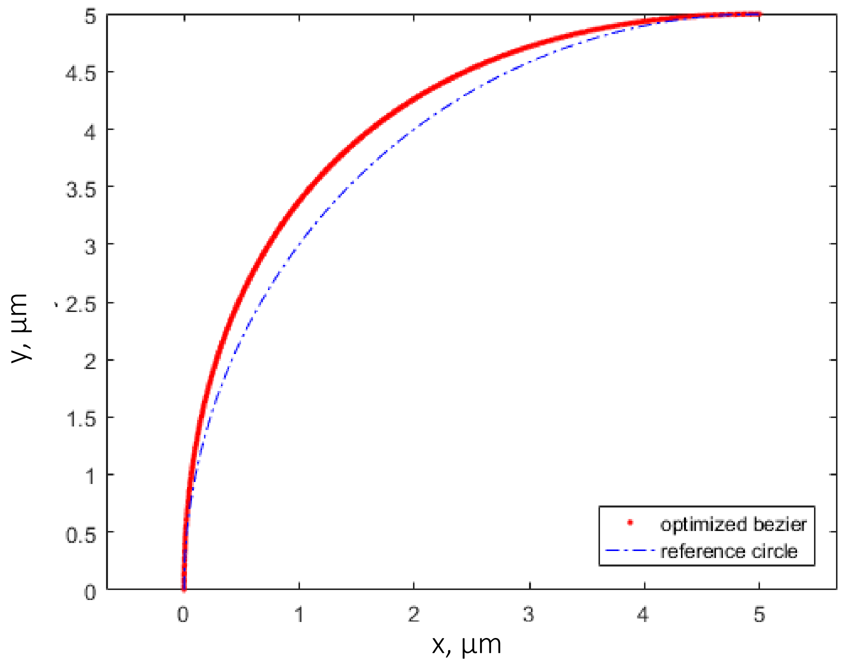

Figure 27 Optimized waveguide bend paths (red) compared to circular arcs (blue) for two device footprints: (a) 1 µm^2 and (b) 25 µm^2.

The geometry of the optimized curves shown above can be explained through a modal analysis of the curved waveguides. As previously discussed, transition losses are incurred when the curvature of the waveguide changes because of the resulting change in the guided mode profile. Therefore, there are no transition losses if the radius of curvature is constant. Meanwhile, bending losses are a function of the instantaneous curvature in the waveguide, as the guided modes in curved waveguides develop an imaginary field component. Naturally, the bend curvature for orthogonal waveguide couplers with a larger footprint is smaller than for those with a smaller footprint. As there is a roughly exponential increase in bending losses with decreasing curvature, this means that bending losses gradually become the dominant loss mechanism as the footprint is decreased.

A similar trend is present for transition losses, but the exponential scaling law for transition losses has a lower exponential factor than that for bending losses, see Figure 28. As a result, the optimized bend structures under compact conditions aim to reduce bending losses at the expense of increasing transition losses by taking on a sub-circular shape. Conversely, for devices with a larger footprint, transition losses are slightly greater than bending losses and this leads to a shape with greater path length than a circular arc.

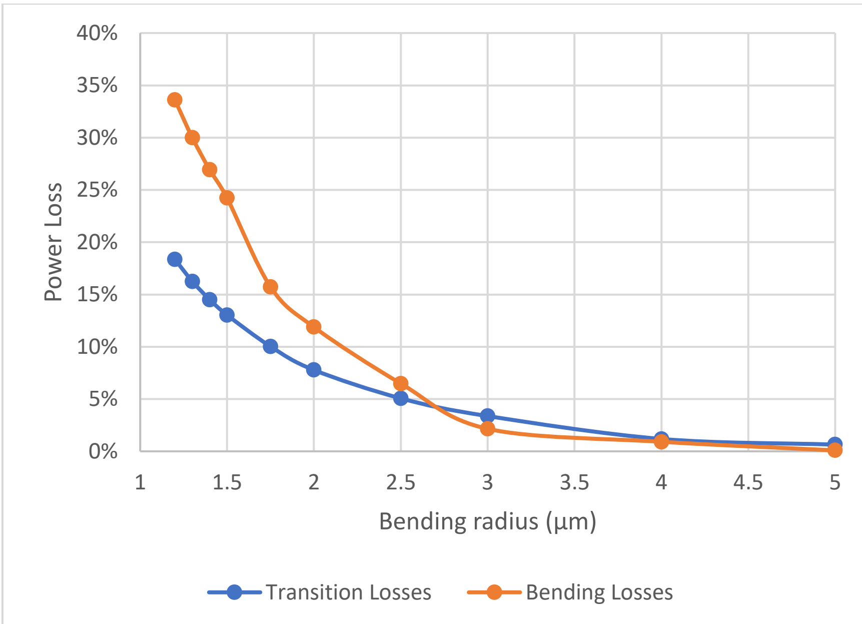

Figure 28 Comparison of transition and bending losses in SOI wire waveguides.

As we have constrained the optimized curves to be symmetric by using the control point relationship in (Eq. 19), another way to quantify the difference between the curves is to look at the distance between their midpoints and the center of the circular arc, labeled as d in Figure 29, and the radius of the circular arc, labelled as r. The ratio of d/r, hereafter called the apex ratio, describes the degree that that the optimized arc is sub- or super-circular. Sub-circular bends, unlike super-circular bends, have d/r apex ratios less than unity;

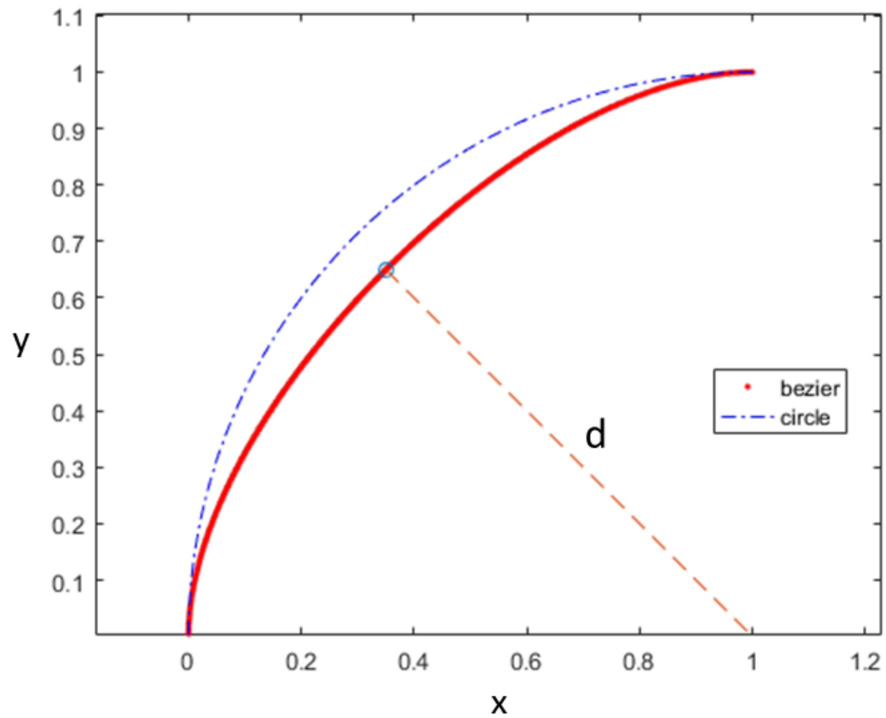

Figure 29 Apex ratio calculation example for sub-circular curve. Here apex ratio is *d* / *r* = 0.92.

Figure 30 shows the change in the total loss (transition plus bending losses) and the apex ratio with increasing one-dimensional device footprint, which is defined as the outside radius of the reference circle arc or the square root of the total footprint. As was the case in earlier waveguide bend studies discussed in the literature review, we see that losses increase roughly exponentially with decreasing bending radius (orange curve in Figure 30). At very small footprints on the order of 1 μm^2, the apex ratio is less than unity, indicating that the optimal shape is sub-circular. The apex ratio increases roughly linearly from 1 µm to around 2 µm, at which point the rate of change decreases. At 1D footprints of ~1.7 µm, a circular arc seems optimal. If the footprint is increased beyond this point larger apex ratios are found, and the optimal curve is super circular. This trend is very similar to the trend in the optimal fitting parameter *a*, which represents the *y* coordinate of the second control point $\mathbf{P}_2$. This relationship is plotted in Appendix D.

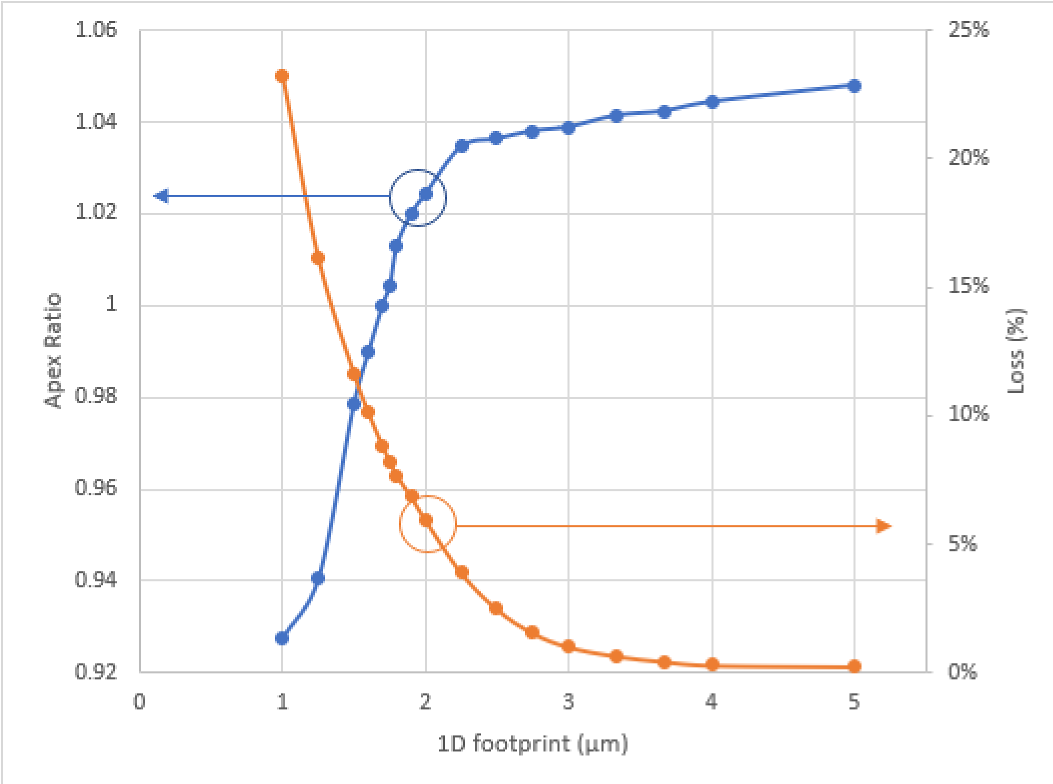

Figure 30 Parameter sweep results for optimized waveguide bend. Apex ratio and loss for 1D footprints between 1 and 5 µm.

The total loss improvement for the optimized structures is of greater interest than the total loss plotted in Figure 30 as it provides information on the potential impact these optimized bends could have on real devices. In Figure 31, the loss improvement of the optimal curve compared to the circular arc is reported as a function of the 1D footprint. Note that the loss improvement approaches zero near 1.7 µm, the point at which the optimized shape was circular. We also see that the use of the optimized Bezier curve has a more significant effect when sub circular bends are optimal. This occurs for more compact waveguide bends, which have worse performance overall. However, near the normal range of operation we also see improvement in transmission on the order of 0.5%. This suggests that using the optimized Bezier waveguide bend could either make circular bends more compact for a given target loss, or that transmission could be improved at the same footprint. For example, consider a typical transmitter receiver photonic integrated circuit with 200 circular 90° bends with a 4 µm radius [50]. If we assume that a 220 nm height SOI wire waveguide is used, similar to the one considered in our modeling work, the optimized results would reduce total losses by nearly 4 dB. Alternatively, a redesigned chip with optimized bends could have the same total loss with an area of only 8.6 µm^2 per bend, which may nearly halve the total chip footprint in some configurations.

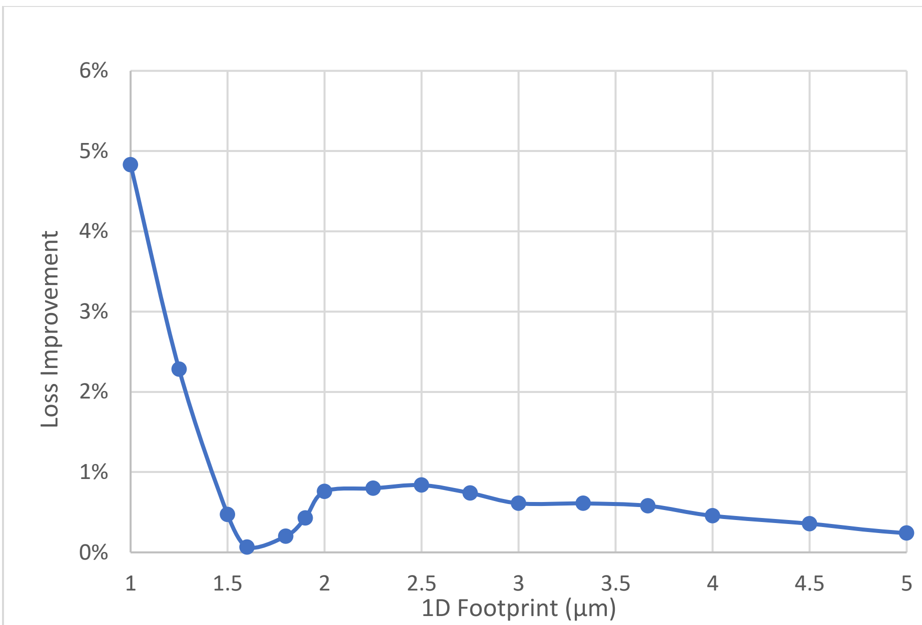

Figure 31 Loss improvement of optimized waveguide bends as a function of 1D footprint.

While the above results show that the symmetric optimization routine yields important improvement in transmission for all tested waveguide bends, it is possible that an asymmetric solution is optimal. To test the symmetric bend assumption, a parameter sweep of the two independent control point coordinates was performed for device footprints of 1 µm^2 and 4 µm^2. The resulting surface for a footprint of 1 µm^2 is presented in Figure 32, alongside a plot of the line containing control points that provide a symmetric Bezier curve. This line is perpendicular to the contour lines of the transmission surface, which are mostly parallel, straight lines throughout the parameter space. This suggests that there is indeed a symmetric curve which provides the optimal orthogonal bend coupler for this device footprint. However, asymmetric alternatives are also available, though they do not result in significant increased performance. Instead, these asymmetric solutions to the optimization problem simply distribute losses differently throughout the structure, as was hypothesized earlier in this thesis. They will have unequal transmission losses at the input and output, and the first half of the waveguide bend will have different bending losses than the second half.

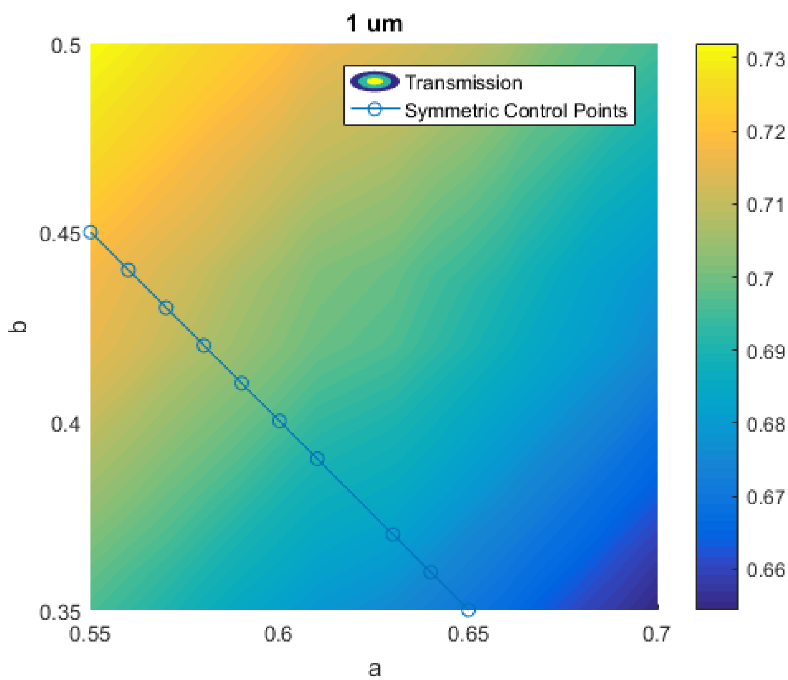

Figure 32 Transmission through Bezier waveguide bend with 1 μm^2 footprint as a function of *a* and *b* parameters for the Bezier curve definition according to Eqs. 17-19.

The parameter surface in Figure 33 for the 4 μm^2 footprint bend structure is very similar to that for a 1 μm^2 footprint. Again, we see that the line of symmetric control points falls mostly perpendicular to the contour lines of the surface, which at first seems to suggest that symmetric solutions exist. However, upon further inspection this trend is not as clear as in the 1 μm^2 surface, as there is a subtle curvature to the contour lines near the maxima in Figure 33. This suggests that if the parameter sweep resolution were increased then it is possible that optimal bend structures could in fact be asymmetrical at this larger footprint. As previously discussed, this could be caused by the fact that bending losses and transmission losses are of similar magnitude for bends with a 4 μm^2 footprint. In this case, there is a slight benefit to skewing the distribution of curvature changes towards the end of the bend where the guided mode will have been slightly attenuated by previous bending losses. Despite this, the benefits of an asymmetric structure are marginal and that nearly optimal behavior is achievable with a symmetric bend.

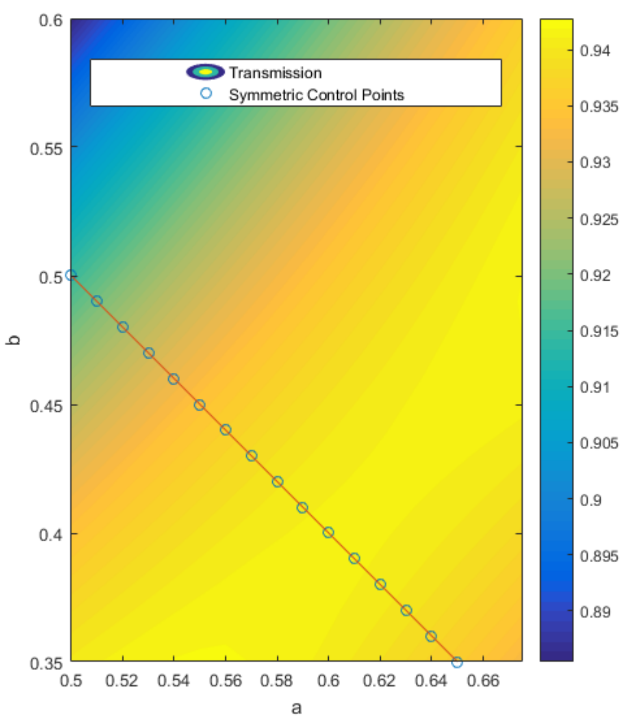

Figure 33 Transmission through Bezier waveguide bend with 4 μm^2 footprint as a function of *a* and *b* parameters.

Summary

Optimized orthogonal waveguide couplers were found by finite difference time domain using a Bezier curve to model the curved waveguide. Overall, the optimized devices performed roughly 20% better than basic circular arcs, making the optimization worthwhile to repeat when designing any photonic integrated circuit that requires multiple bends. A typical transmitter – receiver photonic integrated circuit was analyzed, finding that the optimized bends could either reduce the total curved waveguide footprint by nearly a factor of two, or total losses by between 1 – 4 dB.

The optimized symmetric bend geometries were nearly always non-circular and their geometry depended significantly on the device size. The general trends in optimized bend geometry were quantified through the introduction of the apex ratio, which led to the identification of two distinct regimes of optimized waveguide bend geometries: a sub-circular regime that exists at small footprints and a super-circular regime at the larger footprints that are typically seen in practice. A critical footprint was present at which the optimal bend was circular. For the modeled system, this corresponded to a 2D footprint of roughly 2.9 μm^2. The presence of these two regimes can be well explained through modal concepts of bending and transition losses. Bending losses and transition losses in waveguide bends scale differently as the bend radius is decreased. For bends with large radii the bend losses are comparable in magnitude, but bending losses increase more rapidly when the bending radius becomes very small, below 2 μm for the studied system. As a result, optimized bends for these smaller radii take a sub-circular path in order to reduce the curvature of the waveguide at the expense of increased transition losses.

The larger parameter space of asymmetric couplers was also investigated. Results of this parameter sweep indicated strongly that there exists an optimal symmetric Bezier curve, but that an infinite number of equivalent asymmetric structures could be found. There also may exist conditions where asymmetric solutions are optimal, especially when both transmission and bending losses are significant. Losses are not spread evenly throughout the waveguide bend in these asymmetric curves, meaning that energy may be radiated primarily from a specific part of the waveguide bend. The generation of controlled radiation patterns from optimized bend structures represents a potential area for future investigations, with possible application towards coupling into ring resonators for example.

Conclusion

As photonic technologies increasingly become part of our information infrastructure, optimizing the design of common components such as waveguide bends and tapers can have significant impact. Marginal increases in the efficiency of such structures can greatly improve the performance and cost of the larger system. In this thesis, optimization results and methods for common photonic inverted tapers and bends were presented in order to facilitate their design in future applications, as well as to improve our understanding of the underlying optical processes.

First, a variational treatment of the inverted taper coupler problem was revisited, building upon the initial work on the concept of a constant loss inverted taper by Horth et al [8]. The reasoning behind this finding was further explored through parameter sweeps of coupling loss, primarily to investigate whether the loss functional was indeed convex. Results showed that the step loss was at least locally convex on the typical interval used in practice. Next, parallelizing the constant loss taper simulation allowed for analysis of these structures in a larger, more practical parameter space. New normalization methods were developed as a result, which allowed the geometry of the resulting inverted tapers to be very well described by a global fitting equation, irrespective of the strip waveguide material or height. Furthermore, our analysis led to the definition of cladding and core dominated regimes for mode conversion in tapered waveguides.

Second, the well-studied problem of orthogonal bend coupling was revisited with a focus on the effect of device footprint on optimized waveguide curves. Bezier curves were used to model waveguide bends in FDTD, and a particle swarm algorithm was used to optimize the transmission of these bends for the fundamental TE mode. Overall, a roughly 20% improvement was possible through optimization of curves in orthogonal waveguide couplers. As expected, the performance and geometry of the optimized waveguide bend depended strongly on the permissible device footprint. More specifically, two footprint regimes existed that had distinctly different behavior. At very small footprints optimized bends became sub-circular due to the rapid scaling of bending losses relative to transition losses with decreasing radius of curvature. Meanwhile, larger footprint waveguide bends benefitted from a super-circular shape as this served to decrease transition losses at input and output interfaces. A further finding regarding curved waveguide structures was related to the symmetry of the optimal solution. Two parameter sweeps of the Bezier control points indicated that asymmetric bends could provide the same performance as symmetric bends, which implies that there are an infinite number of optimal curves for any given footprint. This opens the possibility that waveguide bends could be optimized not only for their total loss, but also for a specific radiation pattern.

Overall the two waveguide optimization studies presented in this thesis highlight how theoretical analysis of loss mechanisms in photonic devices can produce novel insights when coupled with massively parallel simulations launched on the cloud. This combination can lead not only to conceptual developments, but also to significant improvements in device performance without sacrificing manufacturability.

Appendix A – Step Reflection and Transmission

Surfaces below show the reflection and transmission occurring at a step discontinuity in a SOI wire waveguide. The values were calculated using overlap integrals derived from coupled mode theory and demonstrate the existence of a global turning point denoted by *w** in (b).

(a)

(b)

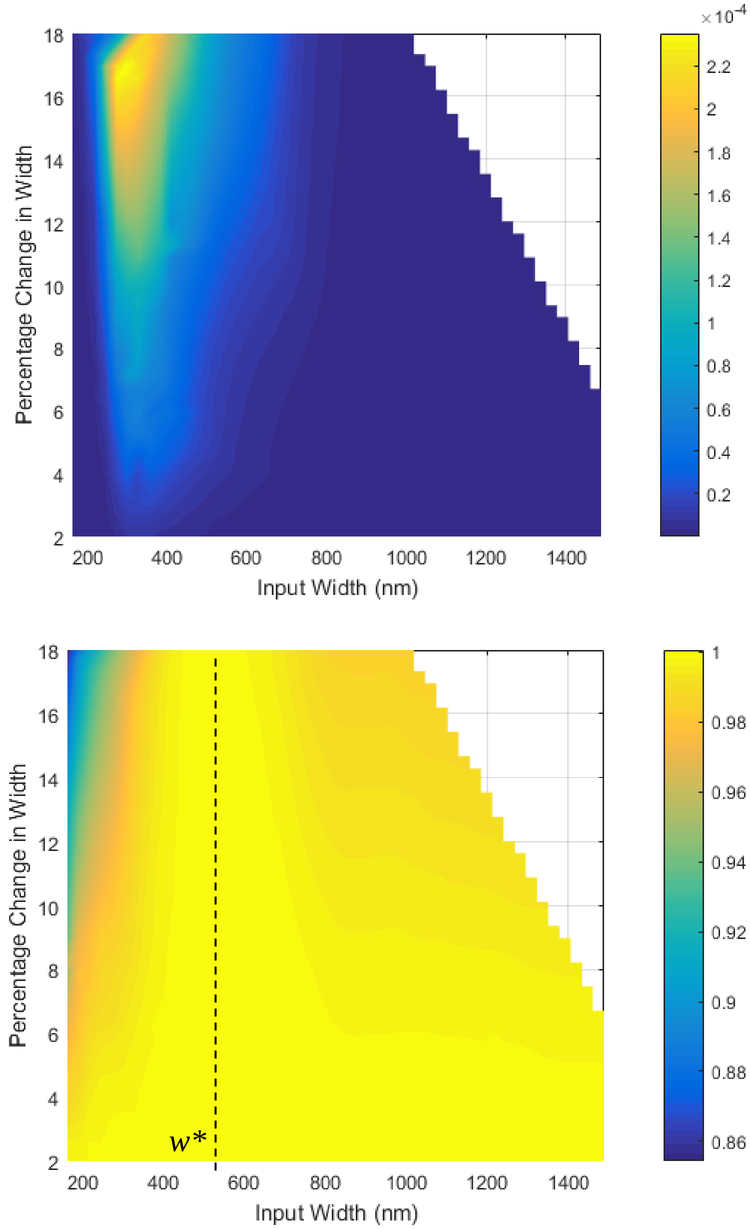

Figure 34 Surface describing effect of a step perturbation in a 220 nm tall rectangular waveguide with core refractive index 3.48 encapsulated in glass cladding with refractive index 1.48 (a) Reflection and (b) Transmission as functions of input and output widths of waveguide step.

Appendix B – Multilinear regression results

The table below provides the multilinear regression results when fitting the parameters in Eq. 14 for the constant loss effective index profile in the optimized inverted taper. The parameters were fitting as functions of the waveguide height (h), cladding index (n_{clad}), and core index (n_{core}). These coefficients can be used to generate surfaces similar to those reported in Figures 15 and 16. The goodness of fit measures are also reported. The variable x_f is discussed in Appendix C.

	Coefficient – k_{clad}	Coefficient - k_{core}	Coefficient - x_f
1.0	-660.32128	-14557.47290	29.49570
h	8.77600	215.19025	-0.45227
h^2	-0.00801	-0.39014	0.00056
h^3	0.00005	0.00104	0.00000
n_{clad}	-0.00001	0.00000	0.00000
$n_{clad} * h$	0.00000	-101.73875	0.26261
$n_{clad} * h^2$	-11.70887	0.07356	-0.00021
$n_{clad} * h^3$	0.01023	-0.00002	0.00000
n_{clad}^2	-0.00060	6565.14002	-17.79270
$n_{clad}^2 * h$	-210.32380	15.53704	-0.03754
$n_{clad}^2 * h^2$	1.62810	-0.01328	0.00004
$n_{clad}^3 * h$	182.62425	-0.59247	0.00104
n_{clad}^3	-0.27334	-4157.34849	9.97854
n_{core}	-21.02128	0.00000	0.00000
$n_{core} * h$	0.00000	-91.08895	0.20725
$n_{core} * h^2$	-1.32284	-0.03210	0.00011
$n_{core} * h^3$	-0.01193	0.00006	0.00000
$n_{core} * n_{clad}$	0.00000	3044.85440	-5.95867
$n_{core} * n_{clad} * h$	1172.70560	36.93373	-0.09589
$n_{core} * n_{clad} * h^2$	3.96589	-0.00526	-0.00001
$n_{core} * n_{clad}^2$	-0.00030	-427.52627	2.14240
$n_{core} * n_{clad}^2 * h$	-249.89620	-1.99338	0.00437
$n_{core} * n_{clad}^3$	-0.05810	544.90618	-1.33918
n_{core}^2	55.08698	3206.16325	-6.38703
$n_{core}^2 * h$	-167.90042	21.47192	-0.04872
$n_{core}^2 * h^2$	0.37438	-0.00053	-0.00001
$n_{core}^2 * n_{clad}$	0.00179	-2140.15136	4.25198

$n_{core}^2 * n_{clad} *h$	-413.37510	-4.28176	0.01327
$n_{core}^2 * n_{clad}^2$	-0.53392	-166.36353	0.30151
n_{core}^3	39.82722	-950.69573	1.86878
$n_{core}^3 * h$	81.15061	-1.47935	0.00342
$n_{core}^3 * n_{clad}$	-0.04763	356.19916	-0.79122
n_{core}^4	-9.47160	67.61316	-0.12252
n_{clad}^4	-7.01075	487.73768	-1.15680
h^4	0.00000	0.00000	0.00000

Goodness of Fit

Variable	k_{clad}	k_{core}	x_f
R^2	0.9328	0.7638	0.9717
Mean Absolute Error	0.0260	0.0514	0.0083
Mean Absolute Standard Deviation	0.0228	0.0411	0.0063

Appendix C – Linear Approximation to CLT Fitting

When either a shorter design cycle or a taper residing primarily in the cladding dominated regime is desired, a simplified approach to deriving the constant loss taper profile may be used. This method involves using the parametric surface to define the CLT profile in the cladding dominate regime as suggested above, but to approximate the change in the waveguide dimension in the core dominated regime after x = 0.5 profile as a straight line. In this case, we must find a new empirical expression for the slope of this line as a function of height and material properties. As all the inverted taper simulations in this study were performed until a final width of 1500 nm, we find the slope of this line m in nanometers is simply found as shown in (Eq. 21), where w^* is the waveguide width at the CLT effective index profile's inflection point. Here x_f is a fitting parameter that represents the normalized x value when the target 1500 nm width was reached.

$$m = \frac{1500 - w^*}{x_f - 0.5} \qquad \text{(Eq. 21)}$$

This parameter was found for each curve in the parameter space of interest. The resulting goodness of fit plot for x_f is shown in Figure 35 ($R^2 = 0.97$) and the surfaces for x_f as a function of height, n_{core}, and n_{clad} are shown in Figure 36. The multi-linear regression results are also presented in Appendix B. Overall this method results in a very high quality multilinear regression but there is some loss of accuracy in the estimated taper width, which may reduce performance. This downside, however, is not very significant as the width expansion is usually very linear after the critical point that divides the cladding and core dominated regimes. In practice, the benefit of this simplified fitting approach is that it avoids the use of the parameter surface for k_{core}, which exhibits the most error, and eliminates the need to run a parameter sweep for the effective index at larger widths, which may prove time consuming to future researchers.

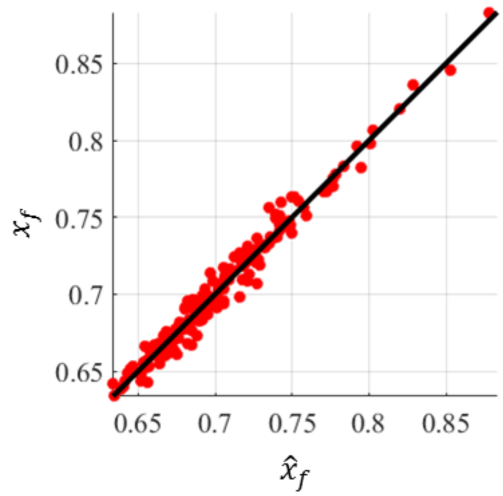

Figure 35 Goodness of fit curve for multilinear regression of x_f.

(a)

(b)

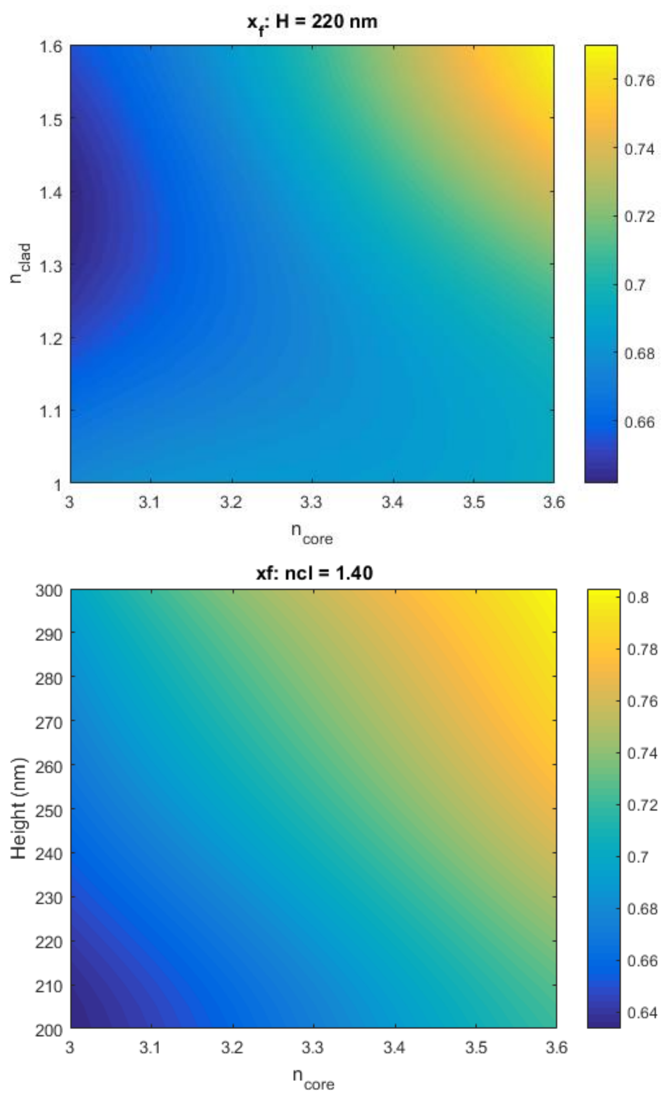

Figure 36 Surfaces for x_f in (a) $n_{cl} - n_c$ and (b) $n_c - h$ search space for cladding index of 1.4

Appendix D – Optimized Bezier Fitting Parameter

The figure below shows the optimized fitting parameter ***a*** for the 90° waveguide Bezier bend as a function of one dimensional footprint, which is the square root of the two dimensional footprint. In the case of a circular bend, this parameter would be roughly equal to the radius. We see in the result below that there is a rapid change in the parameter at small footprints below 2.25 micron.

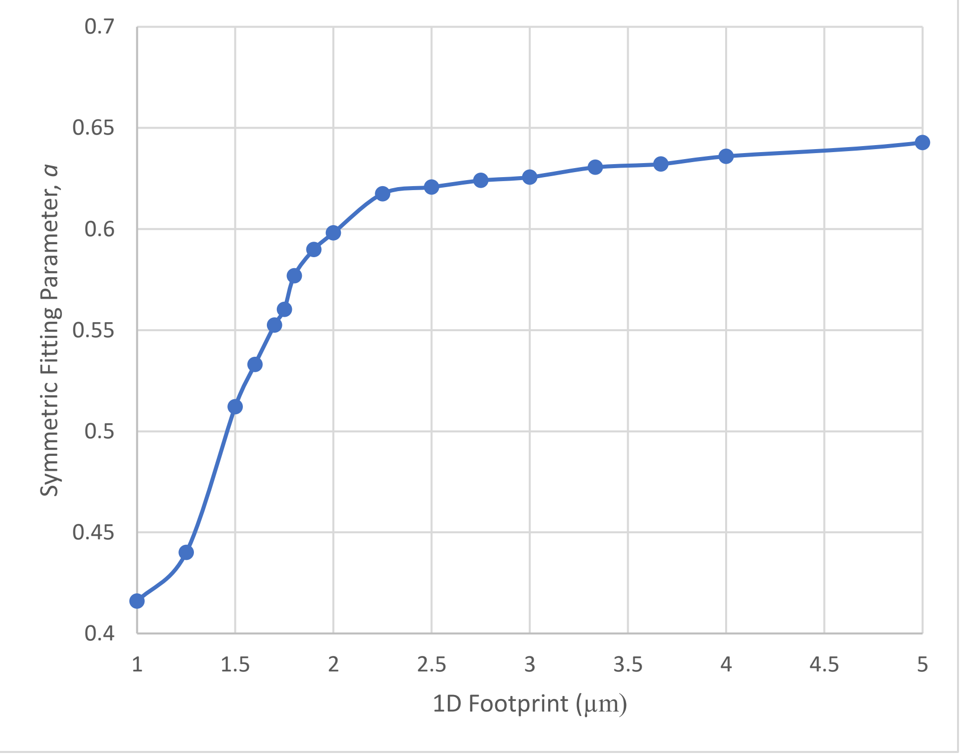

Figure 37 Plot of symmetric Bezier curve fitting parameter *a* against the permissible 1D footprint of an orthogonal bend coupler. The simulated waveguide had a silicon core, a silica cladding, and an input mode wavelength of 1550 nm.

References

1. V. Alwayn, *Fiber-Optic Technologies* (Cisco Press, 2004).

2. A. Al-Azzawi, *Fiber Optics: Principles and Advanced Practices* (CRC Press, 2017).

3. H. H. Hopkins and N. S. Kapany, "A flexible fibrescope, using static scanning," Nature **173**, 39-41 (1954).

4. Hunsperger, *Integrated optics: theory and technology* (Springer, 1984), Vol. 2.

5. A. F. Benner, M. Ignatowski, J. A. Kash, D. M. Kuchta, and M. B. Ritter, "Exploitation of optical interconnects in future server architectures," IBM J. Res. Dev. **49**, 755-775 (2005).

6. G. Lifante, *Integrated photonics : fundamentals* (J. Wiley, Chichester, West Sussex, England; Hoboken, NJ, 2003).

7. P. Cheben, D. X. Xu, and A. Delage, "Scaling Down Photonic Waveguide Devices on the SOI Platform " Proceedings of SPIE **5517**, 147-156 (2003).

8. A. Horth, P. Cheben, J. H. Schmid, R. Kashyap, and N. J. Quitoriano, "Ideal, constant-loss nanophotonic mode converter using a Lagrangian approach," Opt. Express **24**, 6680-6688 (2016).

9. L. Pavesi and D. J. Lockwood, *Silicon photonics* (Springer, Berlin; New York, 2004).

10. T. Shoji, T. Tsuchizawa, T. Watanabe, K. Yamada, and H. Morita, "Low loss mode size converter from 0.3 μm square Si wire waveguides to singlemode fibres," Electronics Letters **38**, 1669-1670 (2002).

11. M. M. Spühler, D. Erni, and J. Fröhlich, "An evolutionary optimization procedure applied to the synthesis of integrated spot-size converters," Optical and Quantum Electronics **30**, 305-321 (1998).

12. V. R. Almeida, R. R. Panepucci, and M. Lipson, "Nanotaper for compact mode conversion," Opt. Lett. **28**, 1302-1304 (2003).

13. B. Luyssaert, P. Bienstman, P. Vandersteegen, P. Dumon, and R. Baets, "Efficient Nonadiabatic Planar Waveguide Tapers," J. Lightwave Technol. **23**, 2462 (2005).

14. W. Westerveld, S. Leinders, J. Pozo, K. W. A. van Dongen, M. Yousefi, and H. Urbach, "Extension of Marcatili's Analytical Approach for 220 nm high waveguides in SOI technology," in *17th Annual Symposium of the IEEE Photonics Society Benelux Chapter*, (Mons, Belgium, 2012).

15. L. Chrostowski and M. Hochberg, *Silicon Photonics Design* (Cambridge University Press, 2015).

16. L. Vivien and L. Pavesi, *Handbook of silicon photonics* (2013).

17. P. Cheben, J. H. Schmid, S. Wang, D.-X. Xu, M. Vachon, S. Janz, J. Lapointe, Y. Painchaud, and M.-J. Picard, "Broadband polarization independent nanophotonic coupler for silicon waveguides with ultra-high efficiency," Opt. Express **23**, 22553-22563 (2015).

18. M. Pu, L. Liu, H. Ou, K. Yvind, and J. M. Hvam, "Ultra-low-loss inverted taper coupler for silicon-on-insulator ridge waveguide," Optics Communications **283**, 3678-3682 (2010).

19. J. Galan, P. Sanchis, W. Bogaerts, P. Dumon, and L. Zimmermann, "V-Groove approach for inverted taper coupling in silicon photonics," in *Technology for Photonics Integration (ePIXnetSpring School'08)*, 2008), 33-33.

20. A. Fenner Milton and W. K. Burns, "Mode Coupling in Optical Waveguide Horns," IEEE Journal of Quantum Electronics **13**, 828-835 (1977).

21. D. Marcuse, "Radiation losses of step-tapered channel waveguides," Appl. Opt. **19**, 3676-3681 (1980).

22. D. Marcuse, "Mode Conversion Caused by Surface Imperfections of a Dielectric Slab Waveguide," The Bell System Technical Journal **48**, 3187-3215 (1969).

23. R. Baets and P. E. Lagasse, "Calculation of radiation loss in integrated-optic tapers and Y-junctions," Appl. Opt. **21**, 1972-1978 (1982).

24. J. Haes, R. Baets, C. M. Weinert, M. Gravert, H. P. Nolting, M. A. Andrade, A. Leite, H. K. Bissessur, J. B. Davies, and R. D. Ettinger, "A Comparison Between Different Propagative Schemes for the Simulation of Tapered Step Index Slab Waveguides," Journal of Lightwave Technology LT **14**, 1557-1569 (1996).

25. D. Gloge, "Optical fiber theory: Opportunities for advancement abound," Radio Science - Wiley (1977).

26. R. Black, S. Lacroix, F. Gonthier, and J. Love, "Tapered single-mode fibres and devices. II. Experimental and theoretical quantification," IEE Proceedings J - Optoelectronics **138**, 355-364 (1991).

27. B. Musa, Y. Mustapha, M. H. Abu Bakar, A. S. Muhammad Noor, A. Ismail, and M. A. Mahdi, "Effects of taper parameters on free spectral range of non-adiabatic tapered optical fibers for sensing applications," Microwave and Optical Technology Letters **58**, 798-803 (2016).

28. D. Marcuse, "Radiation Losses of Tapered Dielectric Slab Waveguides," The Bell System Technical Journal **49**(1970).

29. P. G. Suchoski and R. V. Ramaswamy, "Design of single-mode step-tapered waveguide sections," IEEE Journal of Quantum Electronics **23**, 205-211 (1987).

30. J. Van Roey, J. van der Donk, and P. E. Lagasse, "Beam-propagation method: analysis and assessment," J. Opt. Soc. Am. Journal of the Optical Society of America **71**, 803 (1981).

31. M. M. Spuhler, B. J. Offrein, G.-L. Bona, R. Germann, I. Massarek, and D. Erni, "A Very Short Planar Silica Spot-Size Converter Using a Nonperiodic Segmented Waveguide," J. Lightwave Technol. **16**, 1680 (1998).

32. Z.-N. Lu, R. Bansal, and P. K. Cheo, "Radiation Losses of Tapered Dielectric Waveguides: A Finite Difference Analysis with Ridge Waveguide Applications," Journal of Lightwave Technology LT **12**, 1373-1377 (1994).

33. J. Love, W. M. Henry, W. J. Stewart, R. Black, S. Lacroix, and F. Gonthier, "Tapered single-mode fibres and devices. I. Adiabaticity criteria," IEE Proceedings J - Optoelectronics **138**, 343-354 (1991).

34. C. T. Lee, M. L. Wu, L. G. Sheu, P. L. Fan, and J. M. Hsu, "Design and Analysis of Completely Adiabatic Tapered Waveguides by Conformal Mapping," Journal of Lightwave technology LT **15**, 403-410 (1997).

35. R. Sewell, T. M. Benson, P. C. Kendall, and T. Anada, "Tapered beam propagation," Electronics Letters - IEEE **32**, 1025 (1996).

36. B. Hermansson, J. Saijonmaa, and D. Yevick, "Propagating-beam-method analysis of two-dimensional microlenses and three-dimensional taper structures," J. Opt. Soc. Am. A Journal of the Optical Society of America A **1**, 663 (1984).

37. B. Hermansson, D. Yevick, and P. Danielsen, "Propagating beam analysis of multimode waveguide tapers," IEEE J. Quantum Electron. IEEE Journal of Quantum Electronics **19**, 1246-1251 (1983).

38. H. Yanagawa, T. Shimizu, S. Nakamura, and I. Ohyama, "Index-and-dimensional taper and its application to photonic devices," J. Lightwave Technol. Journal of Lightwave Technology **10**, 587-592 (1992).

39. J. Zou, Y. Yu, M. Ye, L. Liu, S. Deng, X. xu, and X. Zhang, "Short and efficient mode-size converter designed by segmented-stepwise method," Opt. Lett. **39**(2014).

40. M. M. Sisto, B. Fisette, J.-E. Paultre, A. Paquet, and Y. Desroches, "Novel spot size converter for coupling standard single mode fibers to SOI waveguides," in *SPIE OPTO*, (SPIE, 2016), 15.

41. G. Ren, S. Chen, Y. Cheng, and Y. Zhai, "Study on inverse taper based mode transformer for low loss coupling between silicon wire waveguide and lensed fiber," Optics Communications **284**, 4782-4788 (2011).

42. L. Vivien, L. R. Xavier, S. Laval, E. Cassan, and D. Marris-Morini, "Design, Realization, and Characterization of 3-D Taper for Fiber/Micro-Waveguide Coupling," IEEE Journal of Selected Topics in Quantum Electronics **12**, 1354-1358 (2006).

43. C.-W. Liao, Y.-T. Yang, S.-W. Huang, and M.-C. M. Lee, "Fiber-Core-Matched Three-Dimensional Adiabatic Tapered Couplers for Integrated Photonic Devices," J. Lightwave Technol. **29**, 770-774 (2011).

44. Y. Fu, T. Ye, W. Tang, and T. Chu, "Efficient adiabatic silicon-on-insulator waveguide taper," Photon. Res. **2**, A41-A44 (2014).

45. R. T. Rockafellar, "Integrals which are convex functionals. II," Pacific J. Math. **39**, 439-469 (1971).

46. A. Fallahkhair, K. S. Li, and T. E. Murphy, "Vector Finite Difference Modesolver for Anisotropic Dielectric Waveguides," J. Lightwave Technol. **26**, 1423-1431 (2008).

47. J. W. Eaton, D. Bateman, S. Hauberg, and R. Wehbring, "GNU Octave version 4.0.0 manual: a high-level interactive language for numerical computations.," (2015).

48. W. L. Bond, "Measurement of Refractive Indices of Several Crystals," Journal of Applied Physics **36**, 1674-1677 (1965).

49. D. F. Edwards, "Silicon (Si)* A2 **-** Palik, Edward D," in *Handbook of Optical Constants of Solids* (Academic Press, Burlington, 1997), pp. 547-569.

50. A. Horth, "Electronic discussion regarding use of bends in typical SOI tranceiver/receiver devices," in *McGill University*, T. Hokeman, ed. (2017).

51. J. A. Buck, *Fundamentals of optical fibers* (John Wiley & Sons, 2004).

52. K. Kieu, "Lecture 22 Waveguide = Bend Loss," A. S. University, ed. (2015).

53. W. Berglund and A. Gopinath, "WKB analysis of bend losses in optical waveguides," J. Lightwave Technol. **18**, 1161-1166 (2000).

54. R. Nielsen and S. Sorokin, "The WKB approximation for analysis of wave propagation in curved rods of slowly varying diameter," Proceedings of the Royal Society A: Mathematical, Physical and Engineering Sciences **470**, 20130718-20130718 (2014).

55. M. Khanzadeh, M. Malekshahi, and A. Rahmati, "Optimization of loss in orthogonal bend waveguide: Genetic Algorithm simulation," Alexandria Engineering Journal **52**, 525-530 (2013).

56. F. Ladouceur and E. Labeye, "A new general approach to optical waveguide path design," J. Lightwave Technol. **13**, 481-492 (1995).

57. C. Dragone, "Planar waveguide having optimized bend," (Google Patents, 1993).

58. E.-G. Neumann, "Low loss dielectric optical waveguide bends," Fiber & Integrated Optics **4**, 203-211 (1982).

59. E.-G. Neumann and W. Richter, "Sharp bends with low losses in dielectric optical waveguides," Appl. Opt. **22**, 1016-1022 (1983).

60. E.-G. Neumann, "Curved dielectric optical waveguides with reduced transition losses," in *IEE Proceedings H-Microwaves, Optics and Antennas,* (IET, 1982), 278-280.

61. D. Marcuse, "Field deformation and loss caused by curvature of optical fibers," J. Opt. Soc. Am. **66**, 311 (1976).

62. D. Marcuse, "Influence of curvature on the losses of doubly clad fibers," Appl. Opt. **21**, 4208 (1982).

63. D. Marcuse, "Curvature loss formula for optical fibers," J. Opt. Soc. Am. **66**, 216 (1976).

64. E. Marcatili, "Bends in optical dielectric guides," Bell Labs Technical Journal **48**, 2103-2132 (1969).

65. D. Marcuse, "Bend loss of slab and fiber modes computed with diffraction theory," IEEE Journal of Quantum Electronics **29**, 2957-2961 (1993).

66. M. Heiblum and J. Harris, "Analysis of curved optical waveguides by conformal transformation," IEEE Journal of Quantum Electronics **11**, 75-83 (1975).

67. L. Xu and H. Chen, "Conformal transformation optics," Nature Photonics **9**, 15-23 (2015).

68. B. M. Karnakov and V. P. Krainov, "WKB Approximation in Quantum Mechanics," in *WKB Approximation in Atomic Physics*, (Springer Berlin Heidelberg, 2012), pp. 1-30.

69. J. U. N. Lu, S. He, and V. G. Romanov, "A Simple and Effective Method for Calculating the Bending Loss and Phase Enhancement of a Bent Planar Waveguide," Fiber and Integrated Optics **24**, 25-36 (2005).

70. M. K. Smit, E. C. Pennings, and H. Blok, "A normalized approach to the design of low-loss optical waveguide bends," J. Lightwave Technol. **11**, 1737-1742 (1993).

71. K. Kakihara, N. Kono, K. Saitoh, and M. Koshiba, "Full-vectorial finite element method in a cylindrical coordinate system for loss analysis of photonic wire bends," Opt. Express **14**, 11128-11141 (2006).

72. J. Xiao and X. Sun, "A full-vectorial mode solver for bending waveguides by a modified finite difference method based on E-fields in cylindrical coordinate systems," in *Silicon Photonics and Photonic Integrated Circuits II*, (International Society for Optics and Photonics, 2010), 771922.

73. R. T. Schermer and J. H. Cole, "Improved Bend Loss Formula Verified for Optical Fiber by Simulation and Experiment," IEEE Journal of Quantum Electronics **43**, 899-909 (2007).

74. D. Marcuse, *Light Transmission Optics*, 2nd ed. (Van Nostrand Reinhold, New York, 1982).

75. N. H. Vu, I.-K. Hwang, and Y.-H. Lee, "Bending loss analyses of photonic crystal fibers based on the finite-difference time-domain method," Opt. Lett. **33**, 119 (2008).

76. J.-H. Sun and T.-T. Wu, "Propagation of surface acoustic waves through sharply bent two-dimensional phononic crystal waveguides using a finite-difference time-domain method," Physical Review B **74**, 174305 (2006).

77. J.-P. Berenger, "A perfectly matched layer for the absorption of electromagnetic waves," Journal of computational physics **114**, 185-200 (1994).

78. C. Wu, E. A. Navarro, P. Y. Chung, and J. Litva, "Modeling of waveguide structures using the nonorthogonal FDTD method with a PML absorbing boundary," Microwave and Optical Technology Letters **8**, 226-228 (1995).

79. D. M. Sullivan, "An unsplit step 3-D PML for use with the FDTD method," IEEE Microwave and Guided Wave Letters **7**, 184-186 (1997).

80. F. Teixeira and W. Chew, "PML-FDTD in cylindrical and spherical grids," IEEE Microwave and Guided Wave Letters **7**, 285-287 (1997).

81. Y. Hao and C. J. Railton, "Analyzing electromagnetic structures with curved boundaries on Cartesian FDTD meshes," IEEE Transactions on Microwave Theory and Techniques **46**, 82-88 (1998).

82. R. Coccioli, M. Mongiardo, G. Pelosi, and R. Ravanelli, "Design of matched bends in rectangular waveguides by finite element method," International Journal of RF and Microwave Computer-Aided Engineering **6**, 391-398 (1996).

83. R. Jedidi and R. Pierre, "High-order finite-element methods for the computation of bending loss in optical waveguides," J. Lightwave Technol. **25**, 2618-2630 (2007).

84. R. Jedidi and R. Pierre, "Efficient analytical and numerical methods for the computation of bent loss in planar waveguides," J. Lightwave Technol. **23**, 2278 (2005).

85. G. Yuan, *Characterization of integrated optical waveguide devices* (Colorado State University, 2008).

86. J. Wang, C.-W. Wang, Y. Li, F. Zhou, and W.-M. Liu, "The structure optimization design of the organic solar cells using the FDTD method," Physica B: Condensed Matter **405**, 2061-2064 (2010).

87. J. Yamauchi, M. Ikegaya, and H. Nakano, "Bend loss of step-index slab waveguides with a trench section," Microwave and Optical Technology Letters **5**, 251-254 (1992).

88. C. Seo and J. C. Chen, "Low transition losses in bent rib waveguides," J. Lightwave Technol. **14**, 2255-2259 (1996).

89. P. A. Anderson, B. S. Schmidt, and M. Lipson, "High confinement in silicon slot waveguides with sharp bends," Opt. Express **14**, 9197-9202 (2006).

90. M. Harjanne and T. Aalto, "Design of tight bends in silicon-on-insulator ridge waveguides," Physica Scripta **2004**, 209 (2004).

91. R. Coccioli, G. Pelosi, and S. Selleri, "Optimization of bends in rectangular waveguide by a finite-element genetic-algorithm procedure," Microwave and Optical Technology Letters **16**, 287-290 (1997).

92. G. L. Pedrola, "BPM Analysis of Integrated Photonic Devices," in *Beam Propagation Method for Design of Optical Waveguide Devices,* (John Wiley & Sons, Ltd, 2015), pp. 222-299.

93. "Lumerical FDTD Solutions," (Lumerical Inc., 2017).